Nuclear structure and reaction studies at SPIRAL

A. Navin, Francois de Oliveira Santos, P. Roussel-Chomaz, O. Sorlin

Nuclear structure and reaction studies at SPIRAL

A. Navin, F. de Oliveira Santos, P. Roussel-Chomaz‡, and O. Sorlin

GANIL, CEA/DSM-CNRS/IN2P3, Boulevard Henri Becquerel, F-14076 Caen Cedex 5, France

E-mail: `navin@ganil.fr`

E-mail: `francois.oliveira@ganil.fr`

E-mail: `patrica.roussel-chomaz@cea.fr`

E-mail: `sorlin@ganil.fr`

Abstract. The SPIRAL facility at GANIL, operational since 2001, is described briefly. The diverse physics program using the re-accelerated (1.2 to 25 MeV/u) beams ranging from He to Kr and the instrumentation specially developed for their exploitation are presented. Results of these studies, using both direct and compound processes, addressing various questions related to the existence of exotic states of nuclear matter, evolution of new "magic numbers", tunnelling of exotic nuclei, neutron correlations, exotic pathways in astrophysical sites and characterization of the continuum are discussed. The future prospects for the facility and the path towards SPIRAL2, a next generation ISOL facility, are also briefly presented.

‡ Present address: CEA-Saclay, DSM/DIR, F-91191 Gif sur Yvette Cedex, France

1. Introduction: GANIL and the SPIRAL facility

The GANIL facility completed 25 years of operation in 2008. In the early years, the experimental programs focused mainly on the use of intense stable beams and Radioactive Ion Beams (RIB) produced using projectile fragmentation. The LISE spectrometer [1] and the SISSI device [2] were used to produce RIB using the "in-flight" technique. The genesis of the SPIRAL (Systeme de Production d'Ions Radioactifs Accélérés en Ligne) facility was the need to complement the available facilities at GANIL, and open new experimental avenues in Europe with re-accelerated radioactive ion beams. The SPIRAL project was jointly funded by IN^2P^3/CNRS, DSM/CEA and the Regional Council of Basse-Normandie in December 1993. A combination of the ISOL method [3] (Isotope Separation On Line) and the post-acceleration of these secondary beams to energies around 25 MeV/u followed in the foot steps of the facility at Louvain la Neuve [4]. The originality of SPIRAL lies in the exploitation of fragmentation of the broad range of energetic heavy ions available at GANIL, for the production of the ISOL secondary beams. Such an approach, where the projectile rather than the target is varied to produce different radioactive species differs from the use of proton (or light-ion) beams used at the other ISOL facilities [5]. A large collaborative effort between laboratories in France and Europe was established in order to develop and construct the instrumentation required to exploit these beams. The relatively high energies of the re-accelerated beams, in conjunction with the dedicated instrumentation has allowed, as will be seen, to address challenging problems in the field to be addressed.

The number of radioactive atoms created by the ISOL method depends both on the primary beam intensity and the integrated fragmentation cross section. The intensities of the primary beams available at GANIL, (^{12}C to ^{238}U) vary from 6×10^9 to 2×10^{13} pps. These high intensity heavy-ion beams accelerated by the CSS1 and CSS2 cyclotrons (with a maximum energy of 95 MeV/u), shown in Fig. 1, bombard a thick graphite production target (Fig. 2). The Target-Ion Source system (TIS) is located underground inside a well shielded area. The target, where all the reaction products are stopped, is heated mainly by the primary beam up to a temperature of 2000°C. The conical shape of the target permits an optimum distribution of the energy deposited by the beam, especially in the region of the Bragg peak. In cases where the primary beam power is relatively low, a supplementary extra ohmic heating can be added through the axis of the target to maintain the diffusion of the atoms produced. After production and diffusion, the radioactive atoms effuse to the ion source through a cold transfer tube. Most of the non-gaseous elements are adsorbed here leading to a chemical selection. The atoms then enter the 10 GHz permanent-magnet ECRIS (Electron Cyclotron Resonance Ion Source) Nanogan-3, where they are ionized and extracted [6]. The radioactive atoms are ionized up to charge states corresponding to q/m= 0.06 to 0.40. After extraction from the ECRIS, the low-energy RIB (acceleration voltage from 7 kV to 34 kV) are selected by a relatively low resolution separator (Δm/m = 4×10^{-3}) and injected into the CIME cyclotron (Cyclotron pour Ions de Moyenne Energie), constructed as a part
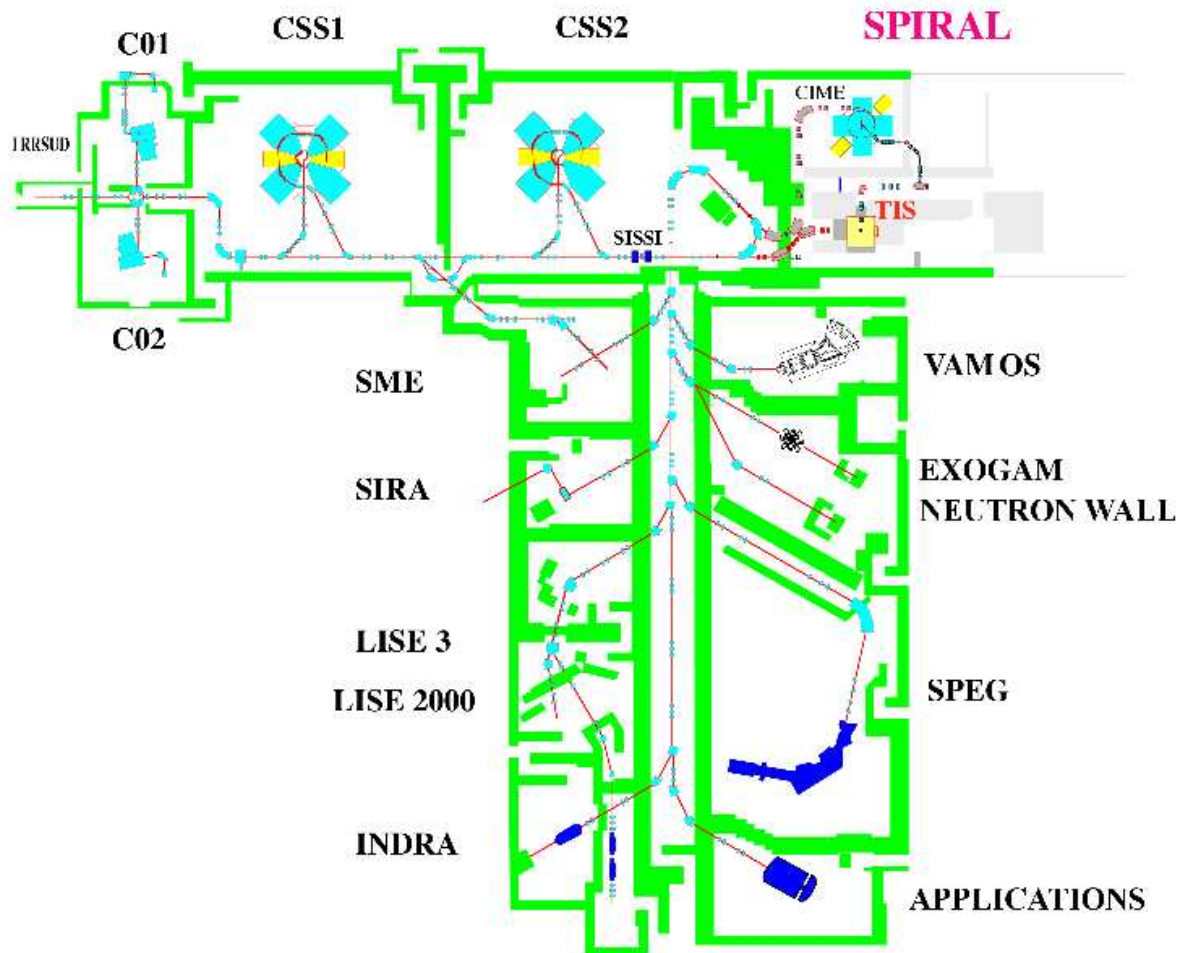
Figure 1. (colour online) A schematic view of the GANIL facility. C01 and C02 are the injector cyclotrons. CSS1 and CSS2 are the sector separated cyclotrons used to accelerate the primary beam which bombards the target ion source (TIS) production system of SPIRAL. The CIME cyclotron is used to post accelerate the radioactive ion beams which are further momentum analyzed before being sent to any of the experimental areas. (The SISSI device has recently been decommissioned).

of the SPIRAL project. In order to test the properties of different target ion source configurations under experimental conditions (limited to a maximum of 400W beam power) a separator SIRa (Séparateur d'Ions RAdiactifs) was constructed in 1993. A detailed layout of the SPIRAL facility and typical SPIRAL targets are shown in Fig. 2. CIME is a room temperature compact cyclotron having K = 265 (Bρ = 2.344 Tm), a magnetic field between 0.75 and 1.56 T and an ejection radius of 1.5m. The beams can be accelerated within an energy range of 1.2 to 25 MeV/u, depending on their mass-to-charge ratio. The beam emittance at the injection is limited to 80π mm-mrad and at ejection to $\sim16\pi$ mm-mrad. The magnet of CIME has 4 return yokes made of thick, stacked slabs. This structure was chosen for its compactness, high field homogeneity and low fabrication cost. The RF resonators are of a classical type with a cantilever dee and a sliding short circuit using spring contacts around the stems. The accelerated RIB
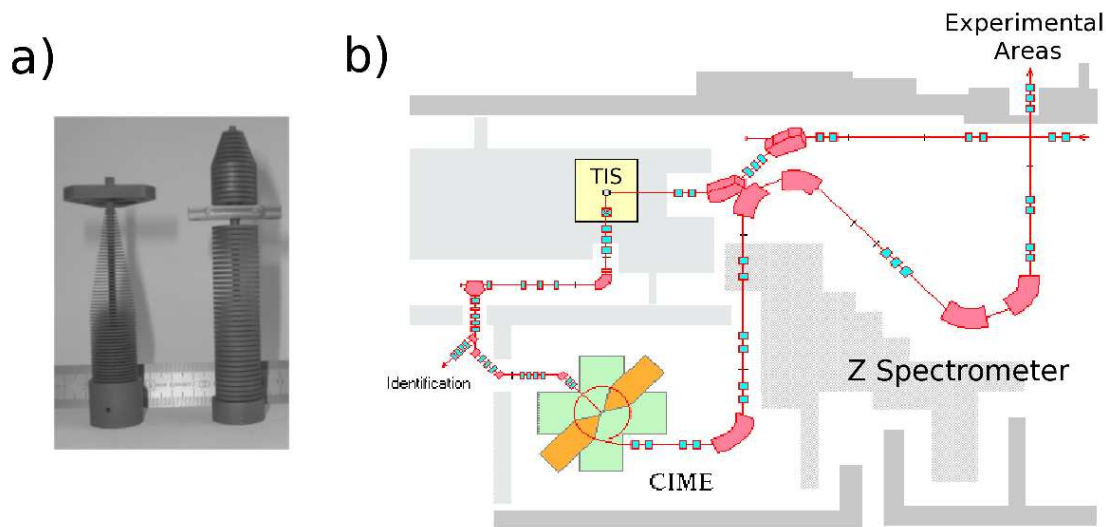
Figure 2. (colour online) a) The SPIRAL graphite targets. b) Detailed schematic view of the SPIRAL facility.

are selected based on their magnetic rigidity by the Z-shaped spectrometer (Fig. 2b) and directed to the existing experimental areas. Specially designed gas profilers and sensitive Faraday cups are used to monitor the profile and intensity of the beams over a wide dynamic range (between 10^3 and 10^7 pps). CIME itself acts as a mass separator with a resolving power greater than $1/2500$. Additional purification can be achieved using a stripper foil to select ions with different masses but having the same mass-to-charge ratio. The first SPIRAL radioactive ion beams were delivered in September 2001. The intensities and variety of beams that are available can be found at: http://pro.ganil-spiral2.eu/users-guide/accelerators/spiral-beams. The operational characteristics of CIME, and the various beams and energies that have been accelerated at SPIRAL are shown in Fig. 3. Because of the chemical selectivity inherent to the TIS, SPIRAL beams were initially limited to noble gases. More recently RIB of Oxygen, Nitrogen and Fluorine have also been produced exploiting the fact that these elements can be produced as molecules in the graphite target. Developments to further extend the available range of elements which can be re-accelerated are in progress. Restrictions arising owing to safety regulations previously prevented the continuous use of the target assemblies, thus substantially limiting the full exploitation of this facility. These safety restrictions were reviewed and relaxed in 2007.

Although a majority of the experimental programs at SPIRAL use post-accelerated ISOL beams from the CIME, experiments are also performed without post acceleration. Precision measurements of the β-ν angular correlation parameter in ^{6}He to search for signatures of physics beyond the standard electroweak model [7], and the measurement of the charge radius of ^{8}He [8], are among the noteworthy results obtained using these low energy (30 keV) beams.

Figure 3. (colour online) The operating characteristics of CIME including the radioactive ion species that have been accelerated.

The present article will first describe briefly the experimental equipment specially constructed to exploit the SPIRAL beams. These include, the large acceptance spectrometer VAMOS, the segmented gamma array EXOGAM, the charged particle detector arrays MUST/MUST2, TIARA and the active target, MAYA. The various physics programs using re-accelerated beams are then described. These include: a) The exploitation of direct reactions to measure and understand the spectroscopy of bound and unbound states in nuclei far from stability; b) Reaction and spectroscopic studies around the Coulomb barrier; c) Selected topics in nuclear astrophysics, probed using resonant elastic scattering and transfer reactions. Finally, the evolution of the facility and its evolution towards SPIRAL2 are briefly presented.

2. Experimental equipment

Intensities of re-accelerated radioactive ion beams, at best four or five orders of magnitude lower than typical intensities of stable beams, necessitate detection devices of a very high efficiency and granularity. The 4π γ-array EXOGAM [9] and the high acceptance, variable mode magnetic spectrometer VAMOS [10, 11] were constructed with several European collaborations. Charged particle detectors
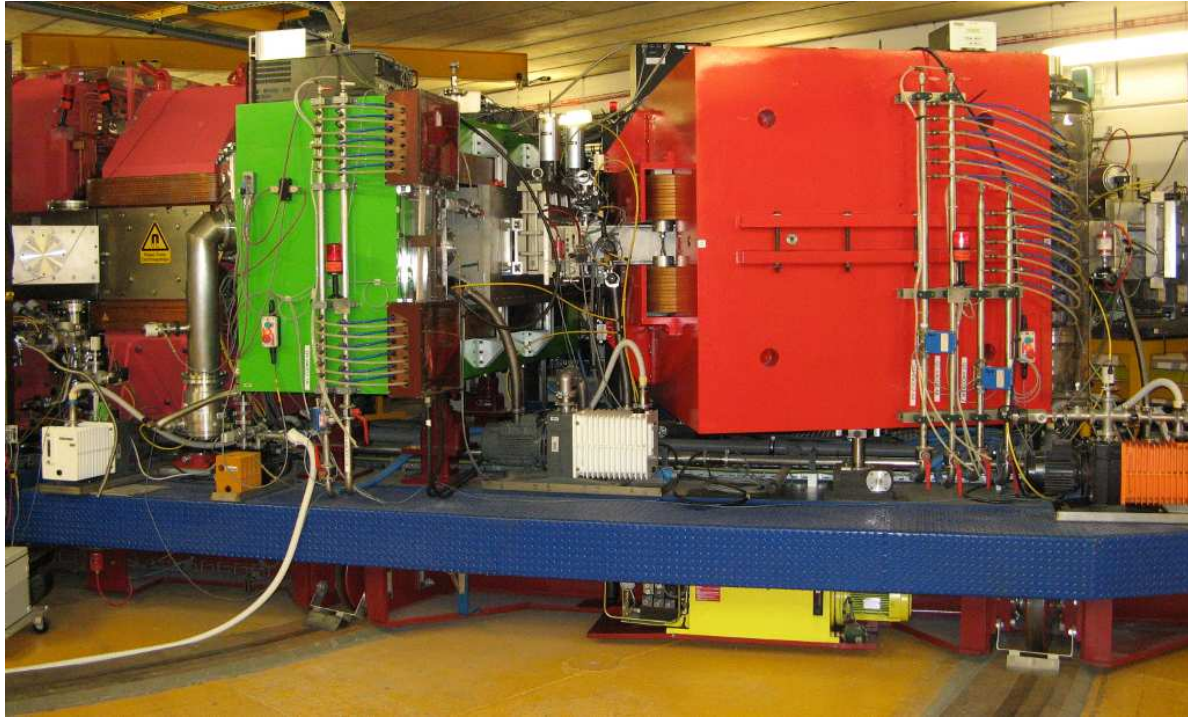
Figure 4. (colour online) The VAMOS spectrometer at GANIL showing (from left to right) the two large quadrupoles, Wein filter, Dipole and part of the focal plane detection chamber.

MUST [12], MUST2 [13] and the TIARA array [14] together with the MAYA [15] active target have been the other major detectors developed to exploit the SPIRAL beams. Related developments in electronics and data acquisition systems have allowed to couple and integrate the above independent detector systems in an optimum manner [16].

2.1. VAMOS

The VAMOS spectrometer (VAriable MOde Spectrometer) [10, 11] is a large acceptance (~ 60 msr) ray-tracing spectrometer. The spectrometer has been primarily designed for a wide range of reactions such as elastic and inelastic scattering, transfer, deep inelastic, fission and fusion evaporation reactions at energies around the Coulomb barrier. The nature and kinematics (conventional and inverse kinematics) of these diverse reactions with stable and radioactive ion beams demand a high performance device that detects and identifies reaction products over a wide range of energies and angles. To meet these requirements, the VAMOS spectrometer combines different modes of operation in a single device. In the momentum dispersive mode of operation, the spectrometer selects and separates the reaction products at the focal plane according to their momentum to charge (p/q) ratio and their unique identification is achieved via an event-by-event reconstruction of the ion trajectory in the magnetic field. This eliminates the need for a position sensitive detector (near the target) to reconstruct the scattering angle and thus allows the spectrometer to also be used at 0°. When operating as a velocity filter at
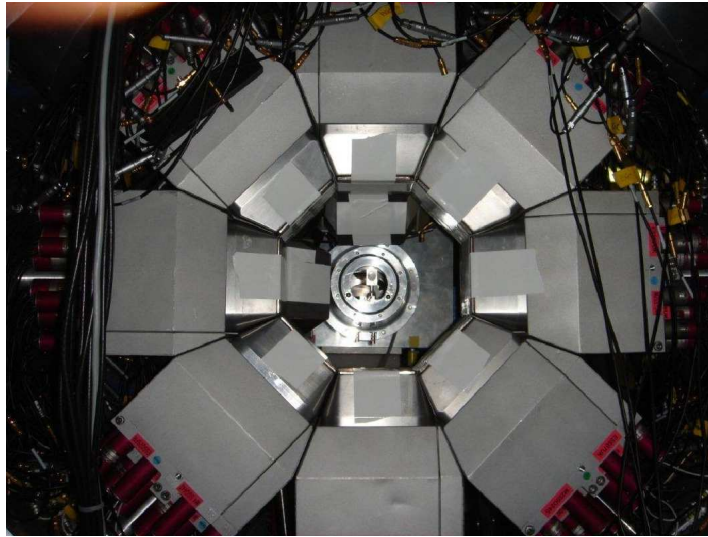
Figure 5. (colour online) The EXOGAM array in a closed packed geometry.

0°, VAMOS separates the reaction products from the direct beam and transports them to the focal plane. The acceptance of the spectrometer has been studied by simulating the trajectory of the particle using an ion optical code. The versatile detection system allows for the unique identification of products (M and Z), ranging from light charged particle to fission fragments arising in collisions induced by both stable and radioactive ion beams from both ISOL and in-flight fragmentation at GANIL [17]. The detectors at the focal plane consist of large area drift chambers, secondary electron detectors, a segmented ionization chamber, and Silicon and Plastic detectors. The spectrometer has a maximum nominal rigidity of 1.8 T-m, Bρ acceptance of $\pm 10\%$, an angular opening of $\pm 7°$, and a flight path of ~ 8 m. The spectrometer can be moved around the target to a maximum angle of 60°. VAMOS is operated in conjunction with a range of detector arrays, including EXOGAM, MUST2, TIARA, INDRA. The VAMOS detection system is presently been upgraded to increase the momentum acceptance of the spectrometer. Recently the spectrometer was successfully operated in a gas filled mode to increase its versatility, especially for experiments requiring the measurement of evaporation residues at 0° [18].

2.2. EXOGAM

The EXOGAM [9] array is composed of up to 16 segmented Compton suppressed Ge clover detectors. It was designed to comply with the special requirements imposed by the use of low intensity radioactive ion beams. Presently the array uses a maximum of 12 detectors. In particular, it was constructed to be a compact, highly efficient and segmented device, most suitable for low multiplicity events. The design also took into account the compatibility with different experimental setups and ancillary detectors. The 16-fold segmentation of each clover detector and the high photo peak efficiency

make it ideal for the search for characteristic γ rays produced in rare events. Photo peak efficiencies at γ-ray energies around 1 MeV are $\sim 1\,\%$ per detector when placed in a closed packed structure (Fig. 5). The high granularity allows correction of the Doppler effect for the gamma rays emitted from fast moving products (typically ~ 20 keV for a 1 MeV gamma ray emitted at $\beta \sim 0.1$). The EXOGAM detector array has been mainly used in two configurations, one which maximizes the efficiency for the EXOGAM array (Fig. 5) and another where the peak-to-total ratio is enhanced with the use of the full Compton suppression to increase sensitivity. An improvement in the position resolution, presently limited by the size of the electrical segment of the crystals was obtained using a pulse shape analysis technique [19]. EXOGAM uses the VXI bus standard developed for the EUROGAM and EUROBALL arrays to operate at high rates [20]. To further improve the performance of this detector array, the signal processing is being upgraded from analog to digital processing. This array is operated in a stand alone mode and also in conjunction with other detectors with both stable beams and RIB (produced in fragmentation reactions or through ISOL methods). It is most often used with VAMOS but has also been used in conjunction with the LISE [1] and SPEG [21] spectrometers.

2.3. Tools for Direct reactions: MUST, MUST2, TIARA and MAYA

New charged particle detector arrays with high efficiency and granularity have been developed to exploit direct reaction studies, taking into account the experimental conditions imposed by re-accelerated RIB. The experiments are performed in inverse kinematics, with the target nucleus playing the role of the light beam in a direct reaction in normal kinematics. The target may either be a thin foil of CH_2 or CD_2 in the case of proton or deuteron scattering, or a cryogenic target of hydrogen or helium. As the nuclei under study are often loosely bound, many states of interest are located above the particle emission threshold and therefore decay in flight, requiring, in principle, the complete kinematic coincidence detection of the ejectile and the decaying particles. The alternative method, used for direct reaction studies with SPIRAL beams, is the missing mass method, where the characteristics of the nucleus of interest are obtained from the kinematical properties of the recoiling light particle in the two-body reaction. The detectors developed include the MUST, MUST2 and TIARA solid state detector arrays and the MAYA active target. Suitable beam tracking detectors were also developed in order to improve the angular definition of the incoming projectiles on an event-by-event basis [22].

2.3.1. MUST and MUST2

The MUST [12] and MUST2 [13] detector arrays consist of 8 telescopes composed of silicon strip, Si(Li) and CsI detectors. These are used for the identification of the recoiling light charged particles through time-of-flight, energy loss and residual energy measurements. The scattering angle is determined from the horizontal and vertical position measurements obtained from the segmented Si strip detectors. The MUST
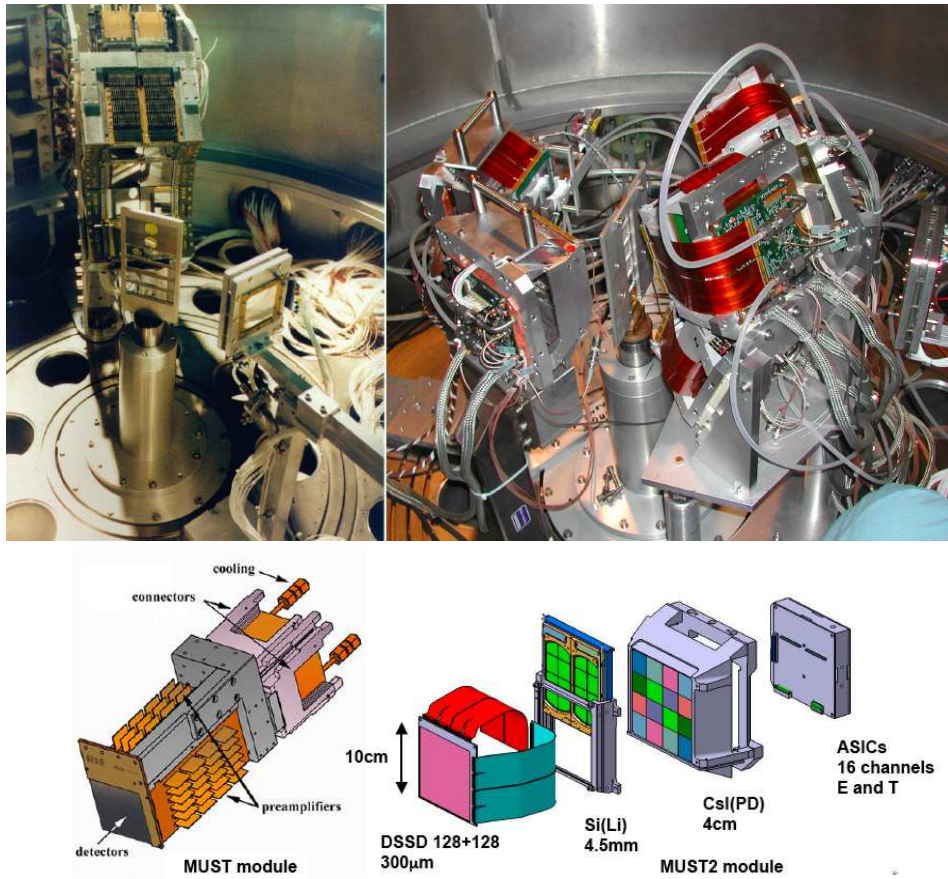
Figure 6. (colour online) Top panel: The MUST (left) and MUST2 (right) detector arrays. Bottom panel: Schematic representations of single modules of the MUST and MUST2 detector arrays.

array was recently superseded by the MUST2 array. The latter has a better angular coverage and resolution, and the smaller volume of the array allows for coincidence experiments with gamma-detectors. Going from MUST to MUST2, the size of the telescopes was increased from 6x6 cm^2 to 10x10 cm^2, the strip size was decreased from 1mm down to 0.67 mm and finally the front-end logic and analog electronics was replaced by a very compact micro-electronics technology (MATE ASIC chips [23]). The 500 μm double-sided strip Si detectors of both arrays have an energy resolution of the order of 40-50 keV, time-of-flight resolution around 1 ns, and an energy threshold of $\sim$ 150 keV for protons. The full energy range covered by the MUST (MUST2) array corresponds to 70 MeV (90 MeV) for protons. These arrays were constructed in a modular manner in order to cover the angular range of interest with a relatively small number of detectors: around 90 deg in the centre-of-mass (c.m.) for elastic and inelastic scattering; at forward angles for pick-up reactions such as (p,d), (d,t), or (d,^{3}He); and at backward angles for stripping reactions such as (d,p). Figure 6 shows images of the MUST and MUST2 arrays, together with schematic representations showing the various components of each
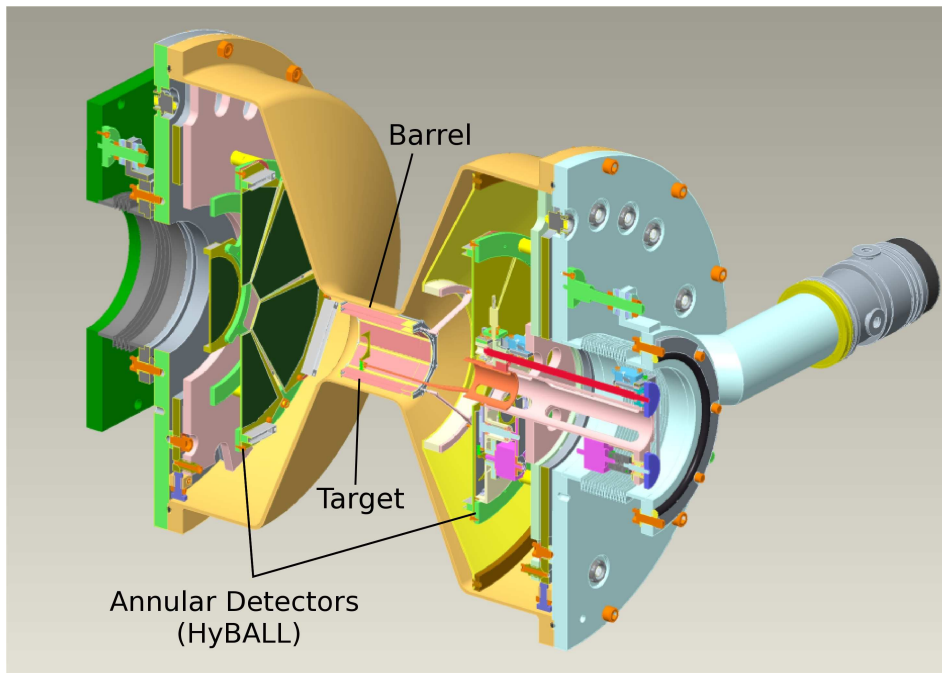
Figure 7. (colour online) A schematic representation of the TIARA detector array.

module for both arrays.

2.3.2. TIARA

TIARA is another compact position sensitive Si array, designed to study direct reactions induced by radioactive ion beams in inverse kinematics. While MUST and MUST2 have been mainly designed to be able to perform inclusive measurements of light particles, TIARA was specifically conceived to be used in coincidence with γ rays detected with EXOGAM and the heavy ejectile in the VAMOS spectrometer. It was constructed within a U.K led collaboration [14]. Figure 7 shows a schematic representation of the array. It consists of 8 resistive strip Si detectors forming an octagonal barrel around the target covering angles between 36° and 143°. Each detector has an active area of about 95mm long and 22.5mm wide, with a thickness of 400μm. The junction side facing the target is divided into 4 longitudinal resistive strips, each with a width of 5.65mm. In total the 32 strips provide azimuthal angles in bins of approximately 9.5 degrees each. In addition, a set of double-sided strip Si annular detectors can be positioned at each end of the barrel detector, complementing the angular range of the barrel. The TIARA reaction chamber has the shape of a longitudinal diabolo, with a central cylinder section of 85mm outer diameter housing the barrel and two 500mm diameter cylindrical sections at each end housing the annular detectors. This geometry maximizes the gamma detection efficiency around the target.

2.3.3. MAYA: An active target

An alternative method of studying direct reactions consists of using an active target
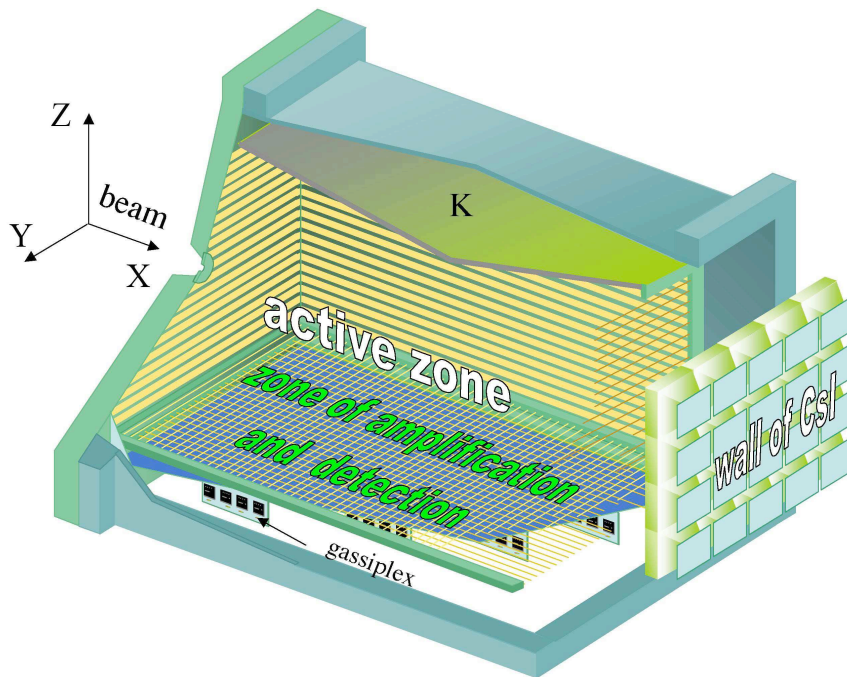
Figure 8. (colour online) Schematic view of MAYA active target including the forward angle CsI wall.

where the gas atoms of the target also act as the detector. An active target in principle has a 4π angular coverage, a very low detection threshold and can have a large effective target thickness without a loss of energy resolution. It is thus ideally suited for the study of reactions as a three dimensional tracking of the reaction partners can be achieved. In the MAYA active target detector (Fig. 8), developed at GANIL [15], the 3-dimensional tracking of the incoming beam and outgoing reaction partners (ejectile and recoiling gas target) is attained via the projection of the charge created on a segmented cathode for the horizontal plane (32 rows of 32 hexagonal pads having a size of ≈ 0.8 cm each), whereas the vertical coordinate is obtained from the drift time measurement on each individual amplification wire with respect to the beam pulse. The induced charge on each cathode pad is measured using the GASSIPLEX chips [24], while the arrival time of the electrons is registered with standard analogue electronics on each amplification wire (one wire for each row of pads). For particles stopped within the gas-volume, the angular and range resolution is determined by the position resolution. Together they determine the energy, the charge and mass resolution. The position resolution is limited to about 1 mm (σ) owing to the combined effects of the pad size and the digitization by the amplifying wires. For particles not stopped in the gas volume, an array of Si-CsI detectors, configured differently for each experiment cover the forward angles. The identification is obtained in this case from the ΔE-E measurement, with energy loss (ΔE) measured in the last section of the MAYA gas volume or in the Si detectors, and

the residual energy (E) in the Silicon or CsI detectors. The detector has also been operated using different gases, including He and CF_4.

3. Direct reaction studies in inverse kinematics to probe bound and unbound states

The role of the nucleon-nucleon (NN) interactions in modifying shell gaps in atomic nuclei is now well established [25]. The most salient feature of these modifications appears in the disappearance of conventional "magic numbers" far from the valley of stability. Transfer reactions such as (d,p) or (d,t) can be used to identify states in nuclei which have a large overlap with pure single-particle states. They thus provide suitable inputs to the understanding of nuclei far from stability, namely: (i) the determination of the in-medium (effective) NN interactions and increasing the predictive power of structure calculations; (ii) the deconvolution of these interactions into central, spin-orbit and tensor terms and identifying the role of each of these in the shell evolution; (iii) the comparison of the properties of "bare" and in-medium interactions to ultimately describe the atomic nucleus from realistic and not purely effective interactions; and (iv) the understanding of the role of the continuum when approaching the drip line.

The (d,p) reaction is used to populate valence neutron orbitals, whereas in the (d,t) reaction a neutron is removed from occupied orbitals. The angular distributions of the measured protons (for (d,p)) or tritons (for (d,t)) provide a signature of the angular momentum ℓ of the final states populated, while the comparison of the measured differential cross sections with model calculations (such as the Distorted Wave Born Approximation or the Coupled Reaction Channels formalisms) quantitatively determines the single-particle strengths (spectroscopic factors). Conventionally, single-particle states have spectroscopic factors (SF) values close to one. Such studies as a function of proton number (for a fixed neutron number) probe the change of energies of neutron single-particle states arising from the proton-neutron V^{pn} interactions (right panel of Fig. 9). Similarly, the evolution of neutron-single particle energies as a function of the neutron number (for a fixed Z) can be used to determine the neutron-neutron interactions V^{nn} (left panel of Fig.9). Examples of this evolution are illustrated in two regions of the chart of nuclides.

Experiments carried out using beams of ^{20}O and ^{24,26}Ne to study the $N = 14, 16, 20$ shell gaps are presented here. This is followed by the use of ^{44,46}Ar beams to probe the $N = 28$ shell gap and the spin-orbit splitting. The analysis of the changes in shell gaps employs principally a shell model approach. The measurements were made at beam energies of $\sim$10 MeV/u where direct transfer is expected to be the dominant reaction mechanism and permits the study of excited states up to $\sim$6 MeV. Additionally, this also favours an angular momentum matching of around $\ell = 2$, which is ideal for the study of the *sdpf* shells. The TIARA [14] and MUST [12] or MUST2 [13] charged-particle arrays were used either independently or together to detect the light charged particles. Tracking of beam particles, where necessary, was made using the position sensitive gas
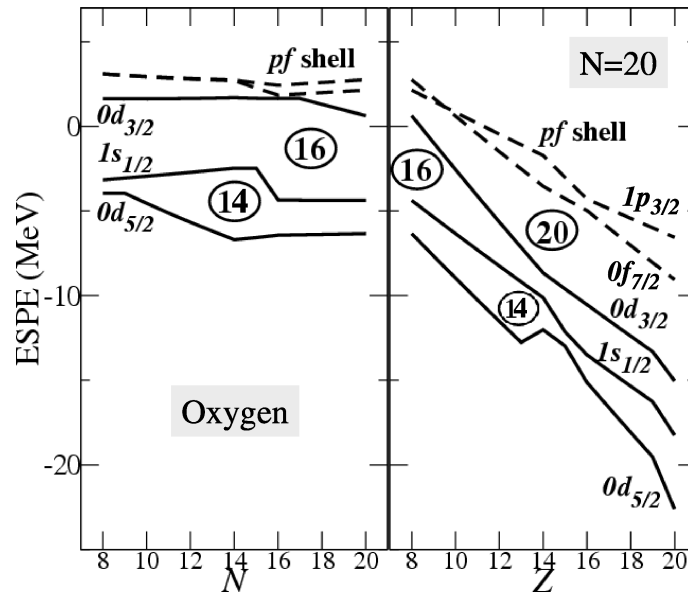
Figure 9. Effective Single-Particle Energies (ESPE) of neutrons in the O isotopic chain (left) and for the $N = 20$ isotones with 8<Z<20 (right) (Refs. [26, 27]).

filled detectors CATS [22]. The SPEG [21] and VAMOS [11] spectrometers were used to select and identify the heavy transfer residues. In some cases, the EXOGAM detectors were used to achieve a better final energy resolution. This also allowed the spin of the states to be constrained using γ-decay selection rules (in addition to the measured transfered angular momentum ℓ).

3.1. Addressing the $N = 14, 16$ and 20 (sub)shell gaps

The variation of Effective Single Particle Energies (ESPE) for the $N = 20$ isotones is shown as a function of the proton number Z in the right panel of Fig. 9. These energies are derived from the shell-model monopole interactions [26, 27], constrained by experimental data available up to 1999. The remarkable constancy of the neutron $N = 20$ shell gap between $Z = 14$ and $Z = 20$, as seen from the figure, indicates the doubly closed shell nature of $^{34}_{14}$Si, $^{36}_{16}$S and ^{40}Ca. For values of Z less than 14 the $N = 20$ gap can be seen to decrease. Therefore, a neutron from the normally occupied $d_{3/2}$ shell can easily be promoted to the higher lying fp shells. Such correlations across the N=20 shell gap lead to the existence of deformed nuclei in the so-called "island of inversion". The disappearance of the $N = 20$ shell gap is caused by the steep change of the neutron $d_{3/2}$ ESPE slope as the proton $d_{5/2}$ orbit is filled. This is a consequence of the largest value of the corresponding monopole term $V^{pn}_{d_{5/2}d_{3/2}}$ in the sd shell. While the $N = 20$ shell gap reduces, a new shell (or subshell) gap is expected to appear at $N = 16$, leading to a new doubly magic nucleus ^{24}O. Despite being smaller in magnitude, an $N = 14$ subshell gap is also present for the $Z = 8 - 12$ nuclei. However, as shown in the left panel of Fig. 9, this subshell gap does *not* exist at $N = 8$ (^{17}O) but appears when

neutrons are added to the $d_{5/2}$ orbital. The strongly attractive $V^{nn}_{d_{5/2}d_{5/2}}$ monopole term increases the binding energy of the $d_{5/2}$ orbit, while the repulsive monopole $V^{nn}_{d_{5/2}s_{1/2}}$ reduces the binding energy of the $s_{1/2}$ orbit leading to a $N = 14$ gap between the $s_{1/2}$ and $d_{5/2}$ orbits. This $N = 14$ subshell gap ($\sim$4 MeV in ^{22}O [28]) leads to ^{22}O$_{14}$ behaving like a quasi-doubly magic nucleus, and accounts for the spherical nature of ^{24}Ne$_{14}$ while ^{20}Ne$_{10}$ is deformed. Finally, the N=28 gap (between $f_{7/2}$ and $p_{3/2}$ orbitals), which is only $\sim$ 2 MeV in ^{40}Ca, is expected to be further reduced at lower Z when the $d_{5/2}$ orbit is empty. These features are addressed in Sects. 3.1.1 and 3.1.2.

3.1.1. The $^{24}Ne(d,p)$ reaction

Measurements were performed using a 10.5 MeV/u ^{24}Ne beam (10^5 pps) on a 1 mg/cm^2 CD$_2$ target. The charged particle array TIARA was used to detect the protons between 100° and 170° with respect to the beam direction. It was used in combination with four segmented clover detectors of the EXOGAM array placed at 90° around the target (with a photo peak efficiency of $\sim$8% at 1 MeV, and $\sim$50 keV resolution after Doppler correction). The heavy transfer residues (^{25}Ne) were detected and identified at the focal plane of the VAMOS spectrometer. The high detection efficiency of the whole system allowed three-fold coincidence data (γ + proton + ^{25}Ne) to be acquired. The measured angular distributions for the observed states are shown in the left panel of Fig. 10. The ℓ values as well as the spectroscopic factors of the corresponding states were extracted from a comparison with Adiabatic Distorted Wave Approximation calculations (ADWA). Combining γ-ray branching ratios, angular distributions and SF values (with uncertainties of $\sim$ 20%) complete spectroscopic information on ^{25}Ne has been obtained and is shown in Fig. 10 [29]).

Also shown in the figure is that the ground state of ^{25}Ne has the expected $\nu s_{1/2}$ configuration, arising from an ℓ =0 transfer with a large SF of 0.8. Significant SF's were also found for the $3/2^-$ (0.75) and $7/2^-$ (0.73) states at 3.33 and 4.03 MeV respectively. The transfer to the "a priori" fully occupied $d_{5/2}$ orbit is still possible, as can be seen from the measured SF value of 0.15 for the $5/2^+$ hole state. A strictly closed shell would have given SF=1 for the $1/2^+$ state and 0 for the $5/2^+$ state at 1.68 MeV. Deviations from these values indicate the possibility of generating neutron excitations across the $N = 14$ gap. The SF for the $3/2^+$ state at 2.03 MeV is about half of that for a pure $d_{3/2}$ single particle strength, the remaining (according to Shell Model calculations) is fragmented between several states at higher energies, each individually having a small SF. Except for the $3/2^+$ state, the energies and SF of the positive parity states are in relatively good agreement with the shell model calculations using the USD interaction [31]. The energy of the $3/2^+$ state was used as a constraint to adjust the monopole terms involving the $d_{3/2}$ orbit in the USD-A and USD-B interactions [32]. The spin assignments for the $5/2^+$ and $3/2^+$ states were ascertained by the fact that only the hole state $5/2^+$ is populated in the one-neutron removal from ^{26}Ne [30]. The salient features of the present work can be summarized as follows : (1) the $N = 14$ gap is relatively large in ^{25}Ne (though smaller than that in ^{23}O by about 1 MeV); (2) the newly observed $3/2^+$ state allows for
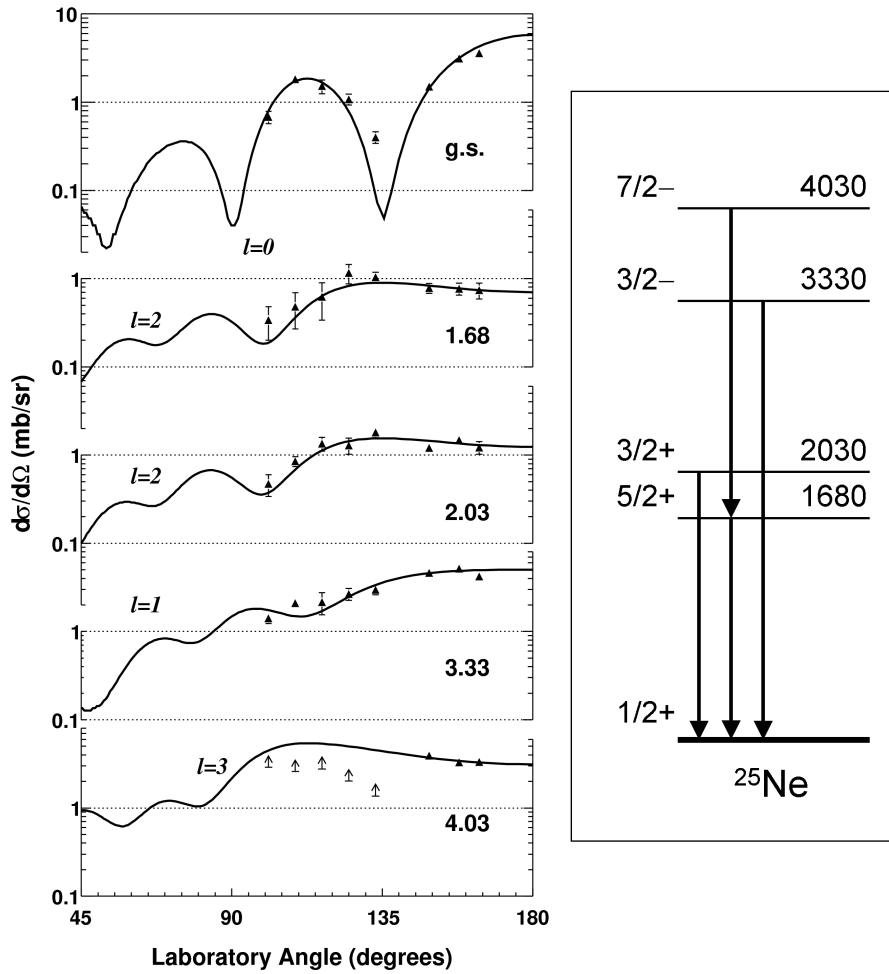
Figure 10. Left: Proton angular distributions for states populated in the ^{24}Ne(d,p) reaction [29]. The spectroscopic factors are noted for each state for the adopted l transfers (solid lines from ADWA calculations). Right: Level schemes deduced for ^{25}Ne [29, 30].

a better determination of the monopole terms involving the $d_{3/2}$ orbit, thus providing for a better understanding of the evolution of the $N = 16$ gap; (3) the $N = 20$ gap formed between the $d_{3/2}$ and intruder fp states seems to be small (about 1.3 MeV); and (4) the $N = 28$ gap, that is 2 MeV in ^{40}Ca, has greatly decreased in the Ne isotopes. This leads to an inversion between the $f_{7/2}$ and the $p_{3/2}$ orbits, as inferred from the energies of the $3/2^-$ and $7/2^-$ states. Note that this inversion was predicted by the ESPE of Fig. 9.

3.1.2. The ^{26}Ne(d,p) reaction

This study provided the first evidence for the presence of an intruder negative-parity state at very low energy in ^{27}Ne. The energies of the excited states in the $N = 17$ isotones, showing the decrease of the $3/2^-$ and $7/2^-$ intruder states with respect to the
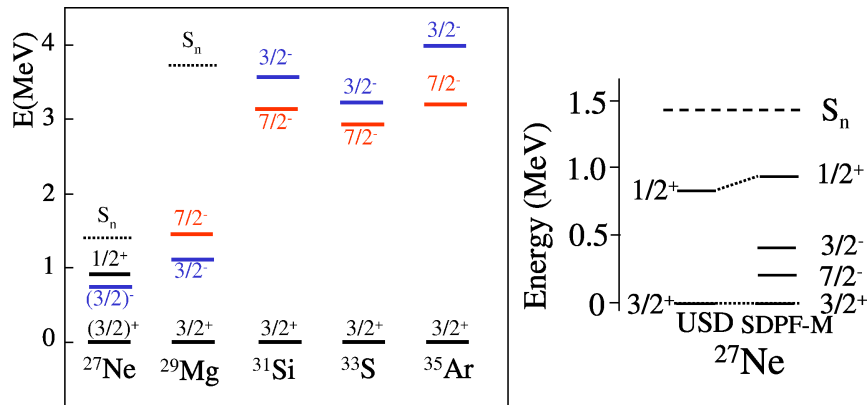
Figure 11. (colour online) Left : Measured energies of the excited states in the $N = 17$ isotones. The decrease in energy of the $3/2^-$ and $7/2^-$ intruder states with respect to the ground state [33] can be seen. Right : Shell model calculations using the SDPF-M interaction [26] for ^{27}Ne. These calculations can account for the presence of intruder states that are outside the valence space of the USD [31] interaction.

ground state are shown in Fig. 11. The ^{26}Ne(d,p)^{27}Ne reaction [33] was performed using a thick cryogenic D_2 target. The transfer to the bound excited states was obtained from the measurement of the Doppler-corrected γ-rays in the EXOGAM array. The transfer-like products were detected in the VAMOS spectrometer. The cross section for the state at 765 keV leads to SF = 0.6 $\pm$ 0.2. This is consistent with the shell model calculations using SDPF-M interaction for a negative parity state ($3/2^-$ or $7/2^-$). A smaller spectroscopic factor, SF = 0.3 ± 0.1, was found for the state at 885 keV for which a spin assignment of $1/2^+$ was suggested based on its excitation energy and spectroscopic factor. Indeed, a relatively small SF for the $1/2^+$ state is expected, as the $\nu s_{1/2}$ orbit is, in principle, fully occupied when pair scattering to the upper $d_{3/2}$ state is negligible. As the protons were stopped in a thick target, angular distribution could not be used to deduce the spin assignments of the observed states. Complementary information on ^{27}Ne from a knockout reaction study is discussed in Ref. [34]. The proton angular distributions from the ^{26}Ne(d,p)^{27}Ne reaction were recently studied using a SPIRAL beam with an intensity of $\sim 10^3$ pps on a thin CD_2 target. The TIARA and EXOGAM detector arrays were used to detect protons and γ-rays respectively. Preliminary results from this work suggest that the $7/2^-$ state is located 330$\pm$80 keV above the neutron-decay threshold (E_x=1.74$\pm$0.08 MeV) [35].

3.1.3. The ^{20}O(d,t) and (d,p) reactions

The combined study of ^{20}O(d,t) and ^{20}O(d,p) reactions provides information on the single-particle energies of both the occupied and valence neutron states at $N = 12$ in the O isotopic chain. This can be compared to the known values at $N = 8$ to derive the evolution of the $N = 14$ and $N = 16$ (sub)shell closures as the neutron number is increased. Additionally, this work can provide constraints on the neutron-
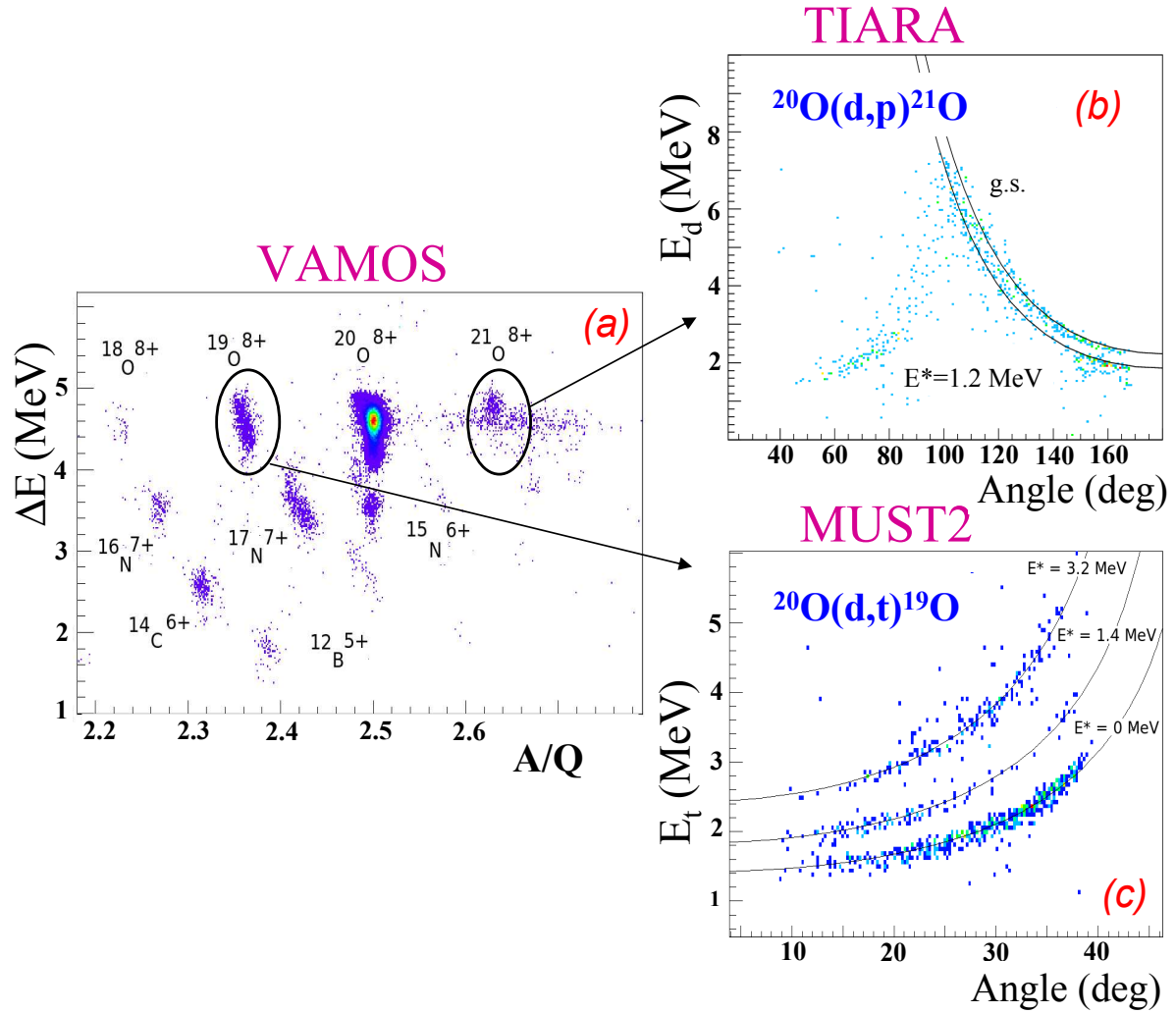
VAMOS

TIARA

MUST2

Figure 12. (colour online) (a) Identification plot of energy loss versus A/Q obtained using VAMOS. The different reaction channels arising from the ^{20}O transfer reactions can be clearly identified. A small contamination of ^{15}N in the beam can also be seen. (b) Kinematic plot of the proton energy as a function of angle in the laboratory frame obtained by gating on ^{21}O in VAMOS. (c) Same as in (b) showing the states in ^{19}O produced by the (d,t) reaction. These preliminary results are from Refs. [36, 37]

neutron interaction involved in the formation of the $N = 14$ gap and contribute to the understanding of the particle instability of ^{28}O.

In this work, the TIARA and MUST2 detector arrays were placed around a CD$_2$ target to detect the recoiling light particles between 36 to 169° and 8 to 36°, respectively. Additionally, four EXOGAM clover detectors were placed in a "cube" geometry around the target, yielding a photo peak efficiency of ∼8% at 1 MeV. A complete identification of all reaction channels was achieved by an unambiguous detection of the heavy products in the VAMOS spectrometer, as shown in Fig. 12a). Detailed analysis and interpretation are in progress, however some preliminary results from Ref. [37] are shown in Fig. 12. Kinematic correlations between the energy and angle of the tritons (Fig. 12c) show

the energies of the states produced in the (d,t) reaction. The lowest lying locus in the ^{20}O(d,t) reaction corresponds to the doublet formed by the ground and an excited state at 89 keV. Gamma-ray measurements indicate that the main contribution to this doublet arises from a transfer to the ground state. Other transitions are identified at $\sim$1400 keV and $\sim$3200 keV. As can be seen in Fig. 12c, the angular distributions of the corresponding levels are quite different. Angular momentum assignments $\ell = 2, 0, 1$ have been derived for the ground + 89 keV doublet, 1400 keV and 3200 keV states, respectively. The energies of the observed states, except for the negative-parity states ($\ell = 1$), which are not in the valence space, are found to be in good agreement with shell model calculations using the USD interaction. The evolution of the energy of the $\ell = 1$ states (from the occupied $p_{1/2}$ shell) may provide information on a possible modification of the size of the $N = 8$ shell gap (between the $\nu p_{1/2}$ and $\nu d_{5/2}$ orbitals) resulting from the neutron-neutron interactions. The values of the SF for the $\ell = 0$ ($1/2^+$) and $\ell = 2$ ($5/2^+$ and $3/2^+$ doublet) states also provide information about the strength of $N = 14$ shell gap in ^{20}O.

Preliminary results on the ^{20}O(d,p) analysis are shown in Fig.12 (b). Gating on ^{21}O, as identified using VAMOS, two clear kinematical lines, which most likely characterize the transfer to $d_{5/2}$ and $s_{1/2}$ bound orbitals, can be seen. A gate on ^{20}O, indicated a broader kinematic line at a higher excitation energy (not shown). This may corresponds to transfer to the neutron unbound $d_{3/2}$ state(s) in ^{21}O. These results will provide further information on the $N = 14$ subshell gap (complementary to the (d,t) data), as well as the location of the $d_{3/2}$ orbit and on the size of the $N = 16$ gap. It could also provide further constraints on the neutron-neutron interactions involving the unbound $d_{3/2}$ orbit, possibly providing a better insight on the role of T=1 three-body forces [38].

3.2. The evolution of the $N = 28$ shell closure

The "magic number" 28, seen in the doubly closed shell nucleus $^{48}_{20}$Ca was attributed to the effect of the one body spin-orbit (SO) interaction. Additionally, the $N = 28$ gap is known to increase by about 3 MeV between $N = 20$ (^{40}Ca) and 28 (^{48}Ca) while neutrons are added to the $f_{7/2}$ orbit. This behaviour arises from the attractive nature of neutron-neutron monopole $V_{f_{7/2}f_{7/2}}$ while the $V_{f_{7/2}p_{3/2}}$ is repulsive [25]. In fact, the mechanism which forms the $N = 28$ gap is the same as that for the $N = 14$ gap shown in the left panel of Fig. 9. It can be viewed by replacing, in this figure, the neutron ($d_{5/2}$, $s_{1/2}$) orbits at $N = 14$ by the ($f_{7/2}$, $p_{3/2}$) orbits at $N = 28$. The evolution of the $N = 28$ shell gap below ^{48}Ca can be linked to the action of the V^{pn} interaction involving protons and neutrons in the sd and fp shells, respectively [25]. The measurements of the ^{44}Ar(d,p)^{45}Ar [39] and ^{46}Ar(d,p)^{47}Ar [40] reactions described here, were used to determine the evolution of intruder configurations ($N = 27$, Sect.3.2.2) and locate single-particle states ($N = 29$, Sect.3.2.1).

3.2.1. Study of the neutron single particle states in ^{47}Ar

The ^{46}Ar(d,p)^{47}Ar reaction was studied using a pure beam of ^{46}Ar ($2 \cdot 10^4$ pps) at 10.2 MeV/u and a 0.38 mg/cm^2 thick CD$_2$ target [40]. The energy and angle of the protons were measured using 8 modules of the MUST detector array [12], which covered polar angles ranging from $110°$ to $170°$ with respect to the beam direction. The transfer-like products ^{47}Ar (^{46}Ar) were selected and identified by the SPEG [21] spectrometer in the case of a neutron pick-up to bound (unbound) states in ^{47}Ar. The measured excitation energy spectrum is shown in Fig. 13. The measurement of the Q-value for the transfer reaction to the ground state of ^{47}Ar allowed a determination of the N=28 gap in ^{46}Ar of 4.47(9) MeV, which is 330(90) keV smaller than that in ^{48}Ca. This reduction occurs as a result of the removal of two protons from the $d_{3/2}$ and $s_{1/2}$ orbits which are quasi-degenerate in energy at $N = 28$.

Assignments of the angular momenta ℓ and SF (or values of the vacancy expressed as $(2J + 1) \times SF$) for the various states identified in the top panel of Fig. 13 were obtained from a comparison of the experimental proton angular distributions with DWBA calculations. From the measured values of the vacancy of the ground state $3/2^-$ (2.44 instead of 4 for a closed shell) and first excited state $7/2^-$ (1.36 instead of 0 for a closed shell), it was inferred that neutron particle-hole excitation are already occurring across $N = 28$ in the ^{46}Ar ground state.

Measured energies and SF in ^{47}Ar (and those in ^{45}Ar [39]) were used to improve the accuracy of the relevant monopole terms as compared to the interaction suggested by Nummela *et al.* [41]. With this new shell-model (denoted SDPF-NR) interaction the ESPE of the $\nu f_{7/2}$, $\nu p_{3/2}$ and $\nu p_{1/2}$ and $\nu f_{5/2}$ orbits were deduced in ^{47}Ar and compared with those in $^{49}_{20}$Ca [42, 43], as shown in the bottom panel of Fig. 13. As compared to ^{47}Ar its isotone ^{49}Ca has two additional protons in the $d_{3/2}$ or $s_{1/2}$ orbitals [44]. The orbits in which the angular momentum is aligned ($\ell_\uparrow$) with the intrinsic spin, such as $f_{7/2}$ and $p_{3/2}$, become relatively more bound than the $f_{5/2}$ and $p_{1/2}$ orbits where the angular momentum and intrinsic spin are anti-aligned ($\ell_\downarrow$). This feature suggests the existence of spin-dependent terms $\tilde{V}$ in the proton-neutron monopole matrix elements. Quantitatively, values of $\tilde{V}^{pn}_{d_{3/2}f_{\downarrow,\uparrow}}$ have been determined to be $\tilde{V}^{pn}_{d_{3/2}f_{5/2}} \simeq +280$ keV (repulsive) and $\tilde{V}^{pn}_{d_{3/2}f_{7/2}} \simeq$ -210 keV (attractive) for the $f_{5/2}$ and $f_{7/2}$ orbitals. In this case, the change of the SO splitting for the f orbitals was tentatively attributed to the action of tensor forces between the $d_{3/2}$ protons and the f neutrons [45, 40]. The change of the SO splitting for the p orbitals was mainly ascribed to the removal of a certain fraction of $s_{1/2}$ protons. As the protons in the $s_{1/2}$ orbital occupy the central part of the nucleus, the change of the neutron p SO interaction can arise from a depletion in central density of the nucleus. This points to the central density dependence of the SO interaction [40, 46], as opposed to what is normally associated with a surface effect. A reduction in the $N = 28$ gap and the SO splitting are further expected in $^{43}_{14}$Si where there are six less protons than in $^{49}_{20}$Ca. This global shrinking of ESPE will reinforce particle-hole quadrupole excitations across $N = 28$ (occuring to some extent in $^{47}_{18}$Ar). The observed shape coexistence between a spherical and deformed state in

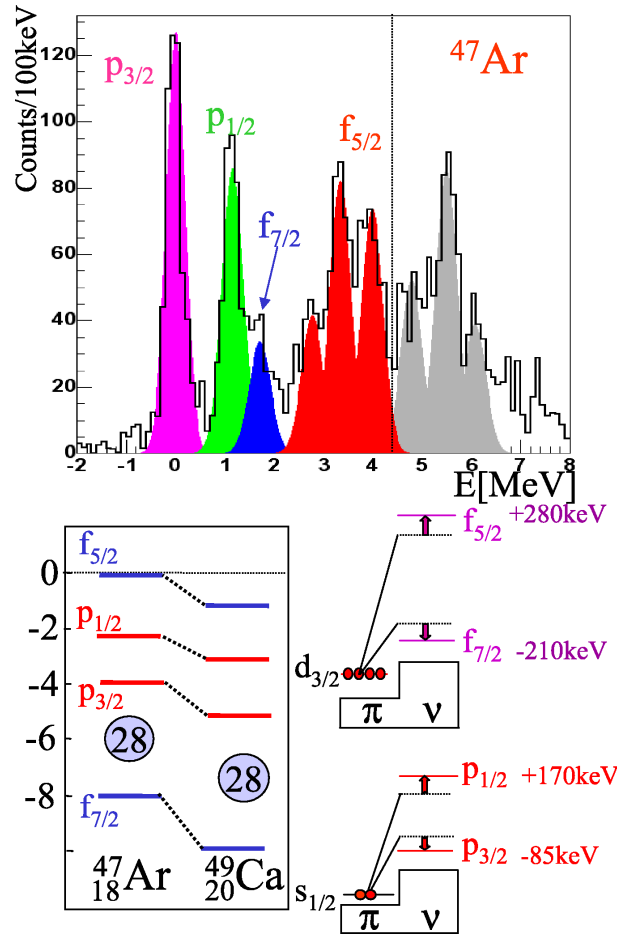**Figure 13.** (colour online) Top: Excitation energy spectrum of ^{47}Ar obtained in the ^{46}Ar(d,p) reaction. The dotted vertical line indicates S$_n$. Bottom left : Neutron Effective Single Particle Energies (ESPE) derived from experimental data for the fp orbitals in $^{47}_{18}$Ar$_{29}$ and $^{49}_{20}$Ca$_{29}$. Bottom Right : Schematic view of the proton-neutron interactions involved in changing the f (top) and p (bottom) SO splittings. For the $p_{1/2}$ and $p_{3/2}$ orbitals, the spin-dependent parts of the total monopole interactions were deduced to be $\tilde{V}^{pn}_{s_{1/2}p_{1/2}} = +170$ keV and $\tilde{V}^{pn}_{s_{1/2}p_{3/2}} = -85$ keV

.

$^{43,44}_{16}$S [47, 48] and the very low 2^+ energy in $^{42}_{14}$Si$_{28}$ [49] confirm this qualitative statement about increased quadrupole collectivity below $Z = 18$ derived from the extrapolation of the ESPE.

3.2.2. Study of intruder states in ^{45}Ar

The ^{44}Ar(d,p)^{45}Ar transfer reaction study [39] was made under similar conditions to those described above. Many new states were populated in neutron transfer and are shown in Fig. 14. Typical energy resolutions (σ) of $\sim$120 keV were obtained. Angular distributions for the first four states in ^{45}Ar are also shown. Unambiguous angular momentum values were deduced for most of the observed levels. In particular, two $3/2^-$ states were found to be populated, the lower one corresponding to the known 550 keV
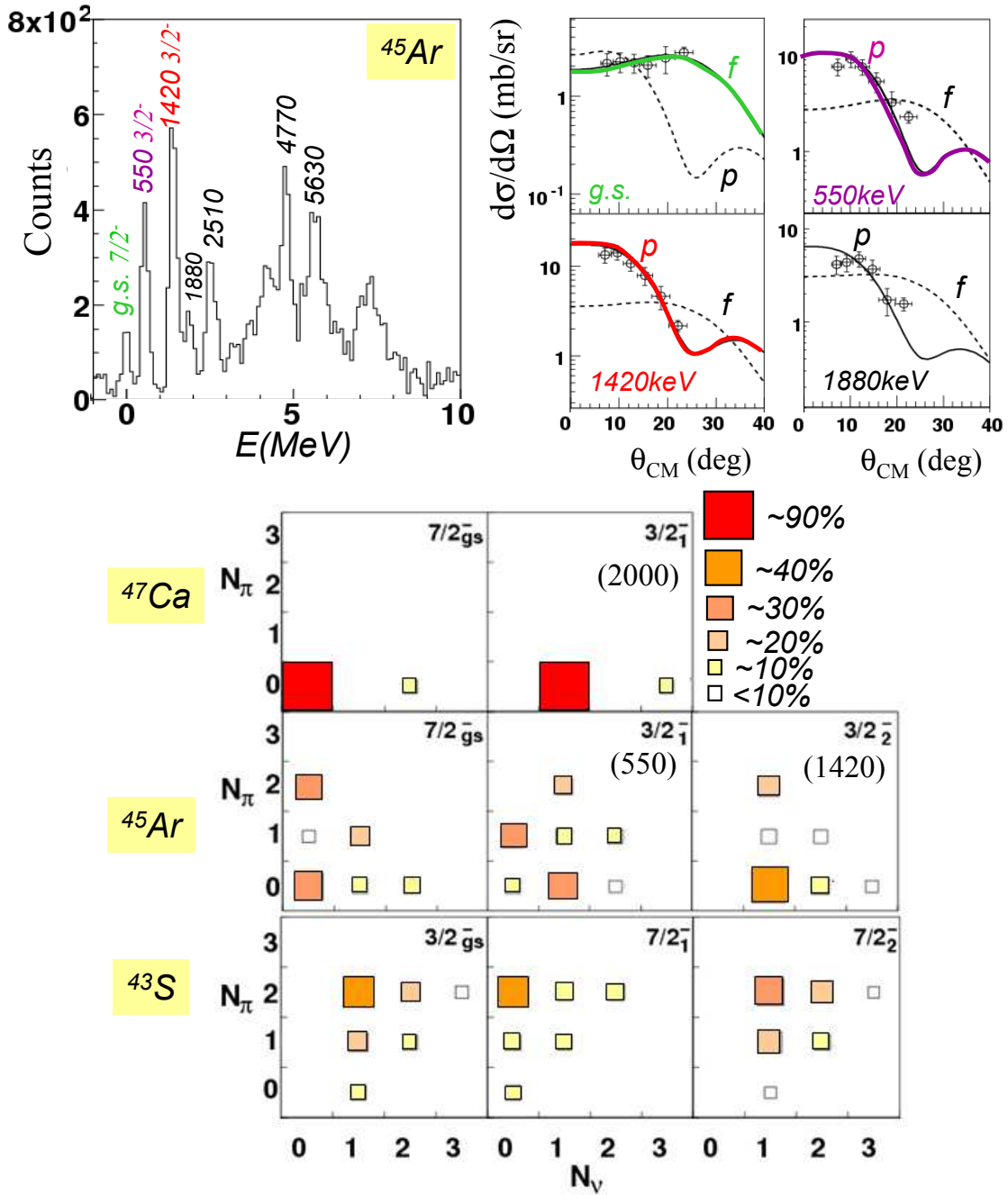
Figure 14. (colour online) Top Left: Excitation energy spectrum of ^{45}Ar obtained through (d,p) reaction [39]. Top Right: Angular distributions corresponding to the four first states are compared to DWBA calculations. Angular momentum values of $\ell = 3, 1, 1, 1$ are derived for the four first states, respectively. Bottom : Configurations of the ground state and excited states of the ^{47}Ca, ^{45}Ar and ^{43}S are compared in term of neutron N_ν and proton N_π excitations.

short-lived isomer Ref. [50].

The evolution of the nuclear structure in the $N = 27$ isotones illustrates how collectivity develops below $Z = 20$. In ^{47}Ca the proton sd shells are completely filled,

giving rise to wave functions for the first two states that have no component of proton excitation (within the proton sd valence space). In addition, the relatively large $N = 28$ gap prevents neutron cross-shell excitations in the ground state. Therefore, the ground state wave function of ^{47}Ca is mainly a neutron $1h$ configuration with respect to the ^{48}Ca core. Combining proton and neutron information, it is found that more than 90% of the ground state wave function of ^{47}Ca contains no proton and neutron excitations, i.e. $N_\pi=N_\nu=0$ (Fig. 14). For similar reasons, the configuration of the first excited state is also relatively pure (Fig. 14). It consists of promoting a neutron into the $p_{3/2}$ orbital ($N_\nu=1$), leaving two holes in the $f_{7/2}$ orbit, giving rise to a $1p2h$ configuration.

In the ^{45}Ar isotone, the wave functions are more mixed (Fig. 14). This occurs for two reasons. First, the proton sd shell is no longer completely filled at $Z = 18$, as such excitations can occur within the sd shells, leading to a proton configuration which extends to one or two proton excitations ($N_\pi=1,2$). Second, neutron excitations across the $N = 28$ gap are favoured as the gap is weakened. The ground state still has a dominant, closed neutron core configuration, having $N_\nu=0$. The second $3/2^-$ state in ^{45}Ar is similar to the first $3/2^-$ in ^{47}Ca. The first excited state (at 550 keV) contains a significant fraction of a recoupling of the $7/2^-$ hole with the 2^+ excitation of the protons. This has implications in understanding the structure of ^{43}S. In ^{43}S an inversion occurs between the normal $1h$ configuration (which is now the first excited state) and the intruder configuration (the ground state) in which one or two neutrons are excited to the $p_{3/2}$ orbit. Having strongly mixed (Fig. 14) but similar configurations, the $3/2^-$ intruder state and the second $7/2_2^-$ state are members of a rotational band. The $7/2_1^-$ has a more spherical configuration. This feature leads to shape coexistence in ^{43}S between the deformed ground state and the spherical first excited state, as discussed in Ref. [47].

3.3. Spectroscopy of light neutron-rich nuclei at the drip line and beyond

Continued experimental effort over the last two decades into studying neutron-rich nuclei in the lowest part of the nuclear chart have revealed the existence of exotic structures, such as halo states and new clustering phenomena. On the theoretical side, "ab-initio" calculations are today able to successfully reproduce properties of light nuclei up to mass 12, starting from the fundamental constituents of the nucleus. However, the treatment of the continuum states and of the cluster phenomenon in such approaches is not yet fully satisfactory, necessitating additional and more detailed data on the lightest nuclei. The study of light neutron-rich nuclei at the limit of the drip line has benefited from the unique ^{6}He and ^{8}He beams produced by SPIRAL at energies between 3 and 25 MeV/u (16 MeV/u for ^{8}He). In particular, the isotopic chain of Helium was extensively studied by means of inelastic and transfer reactions, such as ^{8}He(p,p')^{8}He*, ^{8}He(p,d)^{7}He, ^{8}He(p,t)^{6}He* and ^{8}He(d,p)^{9}He. The most extreme region of the nuclear chart in terms of neutron-proton imbalance was explored, with experiments dedicated to the search for ^{7}H and 4-neutron clusters.
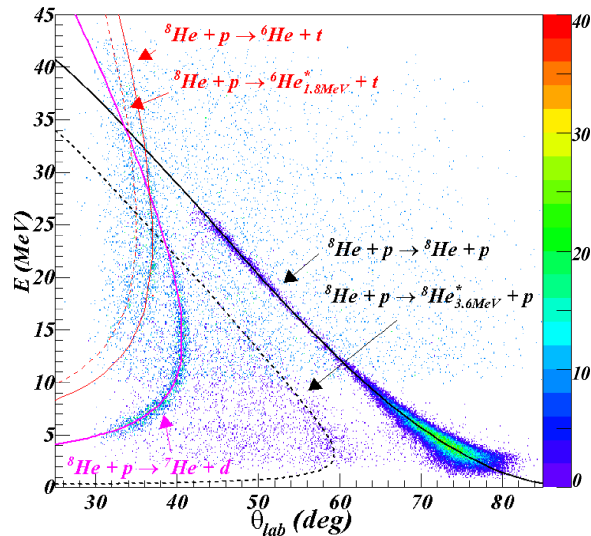
Figure 15. (colour online) Energy-angle correlations for the light target-like recoil, corresponding to elastic and inelastic scattering of ^{8}He on a proton target, ^{8}He(p,d)^{7}He and ^{8}He(p,t)^{6}He* where the recoil is respectively a proton, deuteron or triton.

3.3.1. Spectroscopy of ^{8}He

The nucleus ^{8}He is the particle-stable system with the largest N/Z ratio and exhibits a neutron skin. The first experiment performed with a ^{8}He beam from SPIRAL at 15 MeV/u was dedicated to the investigation of the properties of the four-neutron skin of this nucleus, and to test nuclear structure models at the most extreme values of isospin. Elastic, inelastic and transfer cross sections were measured with the MUST array and compared to theoretical calculations yielding detailed results on the structure of ^{8}He [51, 52, 53]. Figure 15 presents a typical 2-dimensional spectrum showing the energy-angle correlations of the light partner for different reactions induced by a ^{8}He beam at 15 MeV/u on a proton target. The kinematical lines corresponding to elastic, inelastic scattering and to one- and two-neutron transfer reactions can be clearly identified. From the (p,p') analysis, the characteristics of the excited states of ^{8}He were extracted. The first 2$^+$ state at 3.62 ± 0.14 (Γ=0.3 ± 0.2 MeV) and a second state at 5.4 ± 0.5 (Γ=0.5 ± 0.3 MeV) were observed. Theories that include the coupling to the continuum are in agreement with the location of these two resonant states, while other microscopic frameworks (no-core shell model or cluster models) predict higher excitation energies.

Strong coupling effects of the (p,d) and (p,t) pick-up reactions on the elastic scattering were also observed. Several coupled channel calculations were performed using the Coupled Channel Born Approximation (CCBA) [51] and a full Coupled Reaction Channel (CRC) [53], using microscopic or phenomenological potentials. In the CRC calculation, explicit coupling to the (p,d) and (p,t) channels, including the 2$^+$ excited state in ^{6}He and continuum states in the deuteron were taken into account. A consistent description of the three data sets measured with SPIRAL beams together with data at higher incident energies [54] was obtained. The spectroscopic factors extracted from
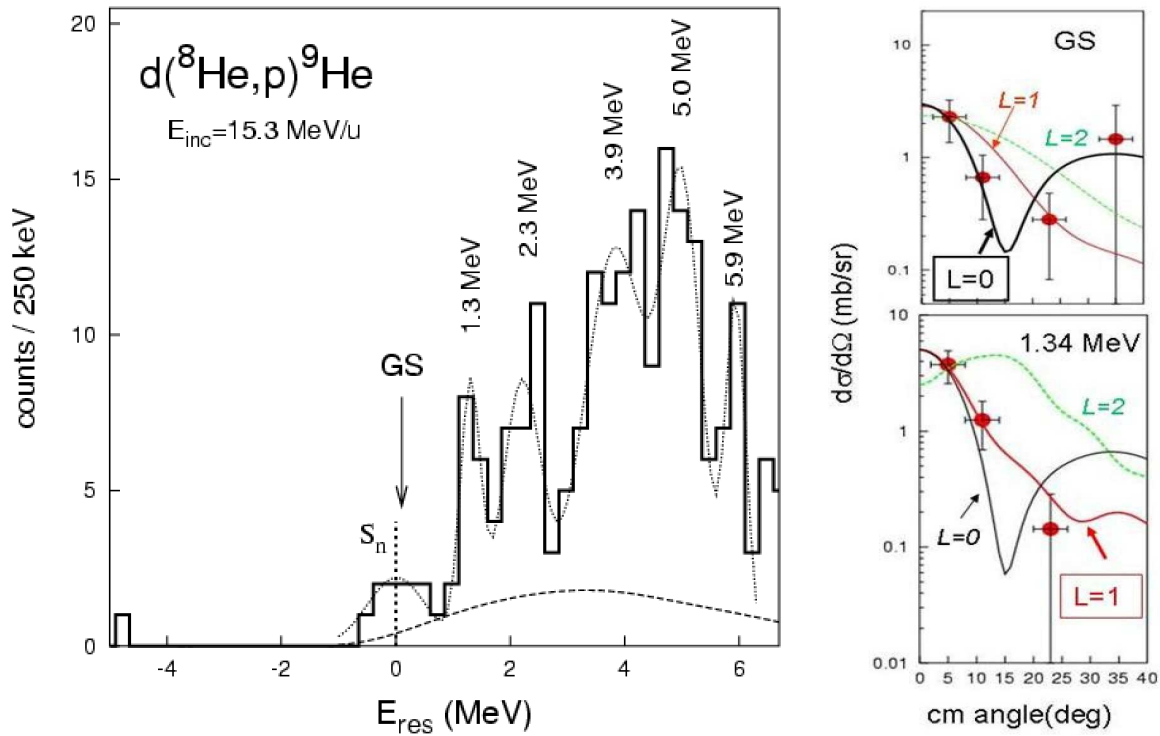
Figure 16. (colour online) Left panel: Excitation energy spectrum of ^{9}He. $E_{res} = 0$ corresponds to the ^{8}He+n threshold. Right panel: Comparison of the measured angular distributions with calculated angular distributions for the states at E=0 and 1.34 MeV.

these analysis for the ^{8}He/^{7}He$_{3/2-}$ and ^{8}He/^{6}He$_{0+}$ overlaps are in good agreement with those obtained in quasi-free scattering [55]. The results of this analysis indicate that while the $(1p_{3/2})^4$ component is probably dominant in the ^{8}He ground state, there is a significant probability of finding the valence neutrons in other configurations such as $(1p_{3/2})^2(1p_{1/2})^2$, contrary to the predictions of the pure jj coupling or of the COSMA model [54]. More recent data obtained using MUST2 confirm these results and allow the exploration of the spectroscopy of ^{6}He at relatively high excitation energy [56].

3.3.2. Shell inversion in ^{9}He

A dramatic evolution of shell structure as function of neutron-proton asymmetry is observed in the N=7 isotones. The energy difference between the s$_{1/2}$ and p$_{1/2}$ orbits is found to decrease going from ^{15}O to ^{11}B, and the level ordering is inversed in ^{11}Be, with the ground state being $1/2^+$ instead of the expected $1/2^-$ assignment. The results obtained from various studies of ^{10}Li find such a parity inversion. Such an inversion can be understood considering the properties of the spin-isospin dependent part of the nuclear interaction [57]. In order to search for a possible p$_{1/2}$-s$_{1/2}$ shell inversion in the next N=7 nucleus, ^{9}He, the ^{8}He(d,p)^{9}He transfer reaction was measured at a beam

energy of 15.3 MeV/u using the MUST array [58]. The nucleus ^{9}He was previously studied using (π^+, π^-), $(^{13}$C,^{13}O$)$ and $(^{14}$C,^{14}O$)$ double charge exchange reactions on ^{9}Be [59, 60]. A narrow resonant state 1.3 MeV above the neutron threshold was identified as the ground state. On the other hand, results obtained from studies using the fragmentation of ^{11}Be [61, 62] were found to be consistent with the existence of a $s_{1/2}$ ground state $\sim$0.1 MeV above threshold. The most recent results, using a knockout reaction, have been obtained at GSI using a 280 MeV/u ^{11}Li beam [63]. A transfer ^{8}He(d,p)^{9}He reaction studies at Dubna [64], showed the presence of two broad resonances located around 2.0 and 4.5 MeV. The analysis showed that these could arise from the interference of the $1/2^-$ resonance with a virtual $1/2^+$ state situated close to threshold and also with a $5/2^+$ resonance above 4.2 MeV.

The missing mass spectrum of ^{9}He obtained from the ^{8}He(d,p)^{9}He reaction study at SPIRAL is shown in the left panel of Fig. 16. This was derived from the energy-angle correlation of the protons at backward angles detected with the MUST array [58]. Despite the rather limited statistics, several peaks can be identified at 1.34, 2.38, 4.3 and 5.8 MeV. The measured proton angular distributions are compared with calculations for neutron transfer to unbound single-particle states made using the DWBA formalism (right panel of Fig. 16) to determine the corresponding transfered angular momentum and spectroscopic factor. The small natural widths (much smaller than single particle estimates) of ^{9}He states previously observed in charge-exchange reactions are unexpected and are in contrast to the broad resonances observed in neighbouring unbound nuclei. The data taken at SPIRAL confirm the existence of the two narrow low-energy resonant states (E=1.34 and 2.38 MeV) reported in Refs [59, 60], but are inconsistent with the broad resonances observed in [64]. Assuming an $l = 1$ transition, the measured spectroscopic factor for the 1.34 MeV resonance is much smaller than 1, indicating a strong fragmentation of the $p_{1/2}$ single particle strength. Regarding the possible $s_{1/2}$ state, the data suggests that the ^{9}He ground state is located just above the neutron threshold (E=0.1 MeV) with $J^\pi=1/2^+$, in agreement with the results of [61]. To improve upon the uncertainties in the angular distributions and l assignment an experiment with improved statistics using the MUST2 detector array has been performed and is presently under analysis. The larger statistics obtained should help in a better understanding of the spectroscopy of ^{9}He.

3.3.3. Superheavy hydrogen ^7H

The system ^{7}H represents the most exotic state of matter, next to that of a neutron star and points towards the question of the number of neutrons that can be held by a single proton. The first tentative evidence for the existence of ^{7}H as a resonance was obtained at RIKEN using the ^{8}He(p,pp)^{7}H reaction at 61.A MeV [54]. A structure just above the t+4n threshold, superimposed on a large background was observed. However, owing to the poor energy resolution (1.9 MeV in the c.m.) the properties of the resonance could not be extracted. The SPIRAL ^{8}He beams were used in two different experiments to measure the properties of this resonance using the missing mass
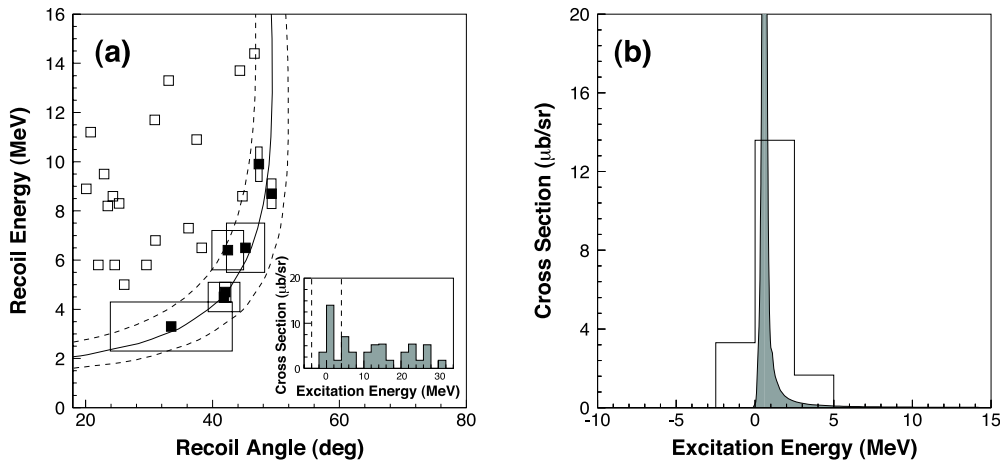
Figure 17. a) Range-angle correlations for the events having a triton in the forward telescopes and an isotope of Nitrogen detected in the MAYA gas volume. The kinematical line for the 2-body reactions leading to ^{7}H is indicated by the full line and the dashed lines correspond to limits of experimental resolution and the width of the resonance. The latter are also shown in the inset which represents the excitation energy spectrum for the various events. b) Excitation energy distribution of the events identified as ^{7}H. The mass of the ^{3}H+4n system corresponds to the zero energy, and the distribution is normalized to the production cross section. The data are represented by the histogram with a 2.5 MeV binning corresponding to the average estimated uncertainty. The solid function is the Breit-Wigner distribution resulting from the fit to the experimental events.

method. The first experiment used the MAYA active target filled with isobutane at 30 mb to measure the ^{8}He(^{12}C,^{13}N)^{7}H reaction [65]. MAYA was used to detect the Nitrogen recoils having a total energy between 3 and 15 MeV. Such low energies prevented the use of a standard solid Carbon target where the recoils would have been stopped for a target thickness compatible with a reasonable luminosity. The events of interest were selected requiring a coincidence between a triton (decay of ^{7}H) in the forward telescopes and a Nitrogen recoil identified in the gas volume of MAYA. The charge resolution obtained on the cathode pads plane was insufficient to identify the mass of the isotopes of Nitrogen produced. Therefore, the selected events could correspond to various isotopes of Hydrogen. However, the kinematics for the different one-proton transfer reactions make it possible to distinguish the various channels. Detailed phase space simulations showed that events corresponding to the formation of ^{7}H nuclear system are located in a region of kinematical correlations that can not be accessed by any other process [66]. The existence of the ^{7}H ground state resonance was therefore confirmed with the identification of seven events where the system was formed with a resonance energy of $0.57^{+0.42}_{-0.21}$ MeV above the ^{3}H+4n threshold and a resonance width of $0.09^{+0.94}_{-0.06}$ MeV (Fig. 17b).

The second result obtained at SPIRAL on ^{7}H was a by-product of the search for 4-neutron clusters (described below) reconstructed by selecting the ^{3}He target-like recoils

detected with the MUST array, corresponding to the proton pick-up reaction ^{8}He(d,^{3}He). The resulting spectrum is shown in Fig. 18, after subtracting the contribution arising from reactions with the Carbon atoms of the CD$_2$ target. The dotted line shows the 6-body phase-space convoluted with the detection efficiency. The existence of a low-lying resonance in the ^{7}H system above the t+4n threshold was confirmed, with a resonance energy of 1.56± 0.27 MeV and a width Γ=1.74±0.72 MeV. The discrepancy between the resonance parameters deduced from the two SPIRAL experiments may be partly due to the poor statistics in these pioneering studies. In addition, one cannot exclude that different states could be populated in the (d,^{3}He) and (^{12}C,^{13}N) reactions.

3.3.4. Search for neutron clusters

The search for neutron clusters has a long history at GANIL [67]. More recently it was triggered by intriguing results obtained in an experiment studying the breakup of ^{14}Be [68]. In this experiment, the neutrons were detected using the DEMON array, in coincidence with charged fragments measured using a Si-CsI telescope placed around zero degree. The analysis revealed the presence of some 6 anomalous events in the neutron detectors, where the deposited energy exceeded significantly the energy deduced from the time-of-flight, assuming the detection of a single neutron. Moreover, these events were found to be in coincidence with ^{10}Be fragments. None were found in the other channels. A detailed study of various effects, including pile up, which could generate such events suggested that the signal was consistent, at the 2-sigma confidence level, with the detection of a bound tetraneutron [68] or a low-lying resonance in the 4n system [69]. In order to further explore these observations, the same method and detection systems were used to investigate the breakup at 15 MeV/u of ^{8}He (an obvious candidate for a tetra-neutron search) supplied by SPIRAL. Unfortunately, owing to a series of technical difficulties in the execution and analysis of the experiment no definite conclusions could be drawn [70].

In parallel, the missing mass method was exploited to address this subject by studying ^{8}He(d,^{6}Li)4n at 15 MeV/u [71]. The MUST array was used to detect ^{6}Li produced by α transfer. Thin Si layers were added in front of the MUST detectors in order to provide an unambiguous identification of ^{6}Li particles. Neutrons were also detected at forward angles using thick plastic detectors in order to improve the reaction channel selection. The excitation-energy spectrum in the 4n system deduced from the ^{6}Li energy-angle correlation is presented in Fig. 18a. This spectrum corresponds to events where at least one neutron has been measured in coincidence with ^{6}Li. Counts observed below the 4n threshold could be ascribed to the background originating from ^{12}C in the CD$_2$ target. Thus, no bound tetra-neutron is observed within the available statistics. Above the α+4n threshold, a smooth increase of the cross section is observed. The data cannot be satisfactorily reproduced by a pure 5-body phase-space calculation, which may indicate the presence of correlations between the 4 neutrons in the exit channel. These correlations have been investigated using simple simulations of 2n-2n interaction in the final state, and the result is shown in Fig. 18 as the solid curve.
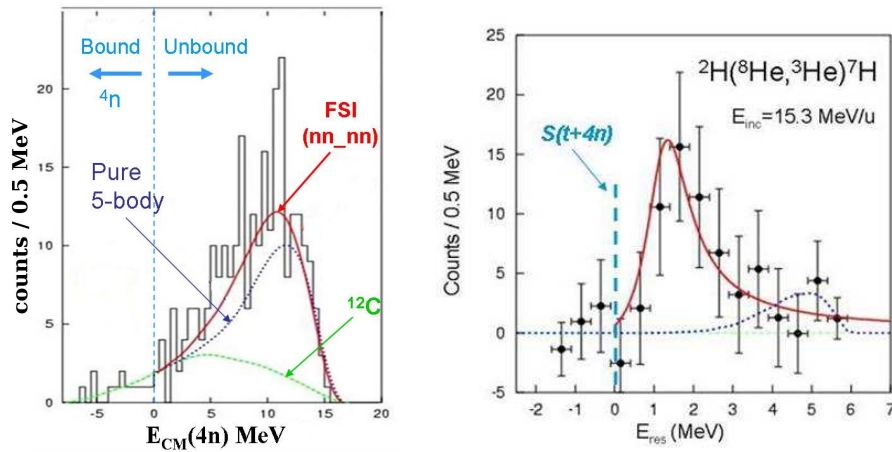
Figure 18. (colour online) Left Panel: Excitation energy spectrum in the 4n system reconstructed from the ^{6}Li particles and gated on a neutron detected in coincidence (see text). Right Panel: Excitation-energy spectrum for ^{7}H obtained from ^{3}He in the same experiment. Zero energy corresponds to the ^{3}H+4n threshold. The resonance energy and width were deduced by fitting a Breit-Wigner line shape (solid line) to the data (see text). The dotted line corresponds to the 6-body phase-space folded with the detection efficiency.

On the theoretical side, state of the art $ab-initio$ calculations lead to the conclusion that a bound tetra-neutron would not be compatible with our present knowledge of nuclear forces [72]. These calculations however cannot yet make reliable predictions concerning the unbound case. Solutions of Faddeev-Yakubovsky equations showed that no physically observable four-neutron resonant states exist [73]. In conclusion, both experiment and theory seem to agree at the present time that bound four-neutron clusters do not exist. The situation is less clear concerning resonances, such states being more difficult to observe especially if they were broad. The results presented in this section push the limits of our present knowledge of the nuclear interaction and structure, and represent the starting point for improving theoretical models, and more generally our understanding of nuclear matter.

4. Reactions and structure studies around the barrier

The reactions of heavy ions at energies around the barrier are governed by a delicate balance between the attractive nuclear and repulsive Coulomb interactions. These studies have conclusively demonstrated that the fusion process cannot be understood as a simple barrier penetration of structureless objects, with a potential depending only on the distance between the centres of the colliding nuclei. The interference between the amplitudes of the many open and virtual channels necessitates the need for treating all the channels in a coherent manner to understand the reaction mechanisms at energies around the Coulomb barrier [74]. These amplitudes can be tuned by changing the beam energy and/or using different projectile-target combinations. Radioactive ion beams

with their weak binding, low-lying continuum states and exotic density distributions open new avenues to probe and understand the effect of these new and interesting features on the reaction mechanism [75]. Additionally, reactions with RIB can be used to produce nuclei which otherwise cannot be produced in reactions involving stable beams. The interest in fusion studies with radioactive ion beams was initially fueled by the conflicting predictions of the influence of weak binding (and thus breakup of the projectile) on the fusion process. One approach treated breakup as causing an attenuation of the flux in the incident channel. The transmission coefficients for fusion are thus multiplied by a breakup survival probability leading to smaller fusion cross sections. This implies that the two channels, the elastic and the breakup products, can fuse incoherently leading to complete and breakup fusion, respectively. In contrast to this intuitive approach, the role of breakup can be considered in a coupled channel formalism like an inelastic excitation to the continuum. This would mean that the fusing system is a coherent superposition of the elastic and breakup channels. It now understood that the effects of coupling to continuum states have to be treated in a coherent manner. The role of such a coupling is to enhance (with respect to a one dimensional barrier penetration calculation) the complete fusion cross sections below the barrier and reduce it above the barrier [76]. In this section we focus on the exploitation of relatively high intensity beams of Borromean systems ^{6,8}He at energies around the barrier to understand multidimensional tunnelling and to study neutron correlations. The exploitation of in-beam and off-beam gamma decay of the residues produced in reactions with relatively low intensity RIB to measure absolute cross sections is also discussed.

4.1. Complete reaction studies

A comprehensive understanding of low-energy reactions with weakly bound projectiles requires an unambiguous identification of the residues produced by different mechanisms and measurements of the respective cross sections. In studies of fusion with weakly bound neutron-rich nuclei, in addition to the total capture of the projectile by the target and the breakup of the projectile, capture of the loosely bound particle(s) by the target is also important. Studies performed at SPIRAL have shown that the cross section for the capture of the neutron(s) is large and arises from a direct process (transfer) [77]. These events (transfer) lead to nuclei which, in the case of medium mass targets, can also be formed after evaporation in a complete fusion process. This emphasized the need for identifying the mechanism of residue production (direct or compound) in reactions involving light neutron-rich RIB in order to uniquely identify the process of complete fusion. Similar issues exist when the fusion cross section is obtained from the measured fission cross section, where the fusion-fission events have to be differentiated from transfer induced fission [78]. This is not the case with heavier non fissioning compound systems which decay mainly by the emission of neutrons. Thus, in general, it is incorrect to equate the total residue (or fission) cross section with the

fusion cross section.

Results for fusion, transfer, breakup and elastic scattering of ^{4,6,8}He on (medium mass) Cu and (heavy) Os and Au targets near the Coulomb barrier were used to address the above mentioned issues. The feasibility of measuring small absolute cross sections using inclusive in-beam γ-ray measurements with low intensity ISOL beams in conjunction with highly efficient arrays was also demonstrated [77, 79]. The neutron transfer process led to the same residues as those formed in the decay of a compound nucleus in a fusion process. These were identified and separated using various measurements of compound and direct processes. Neutron transfer cross sections were measured and found to be larger than those for the breakup of the projectile. This work was the first to a) point out the importance of identifying and delineating the mechanisms of residue formation for understanding fusion with RIB and b) demonstrate the importance of transfer reactions with weakly bound nuclei [77, 80, 81]. With available ^{8}He beams a complete study of all the reaction channels were also performed in the ^{8}He+^{65}Cu systems at energies above the barrier. These measurements further improved upon the sensitivity of in-beam measurements using re-accelerated ISOL beams studies by another two order of magnitude as compared to the results with ^{6}He.

4.2. Neutron correlations in ^{6}He

Neutron-rich nuclei near the drip line, especially Borromean nuclei (bound three-body systems with unbound two-body subsystems), such as ^{6,8}He, ^{11}Li and ^{14}Be, offer a unique environment to study neutron correlations and pairing at low densities. The latter is a necessary input for nuclear structure models and the study of neutron stars. Theoretical studies indicate showed that at low neutron density strong spatial di-neutron correlations maybe expected [82]. It is hoped that the study of the transfer of 1n and 2n will provide signatures for the nuclear equivalent of the Josephson tunnelling [83]. A related question is whether these weakly bound valence neutrons behave as independent particles or as a pair. The ratio of the 2n/1n transfer cross section could provide information about the spatial correlation of the valence neutrons. In ^{6}He the cigar-like configuration, where the two neutrons lie on opposite sides of the nucleus, should preferentially populate ^{5}He by a 1n-transfer while the di-neutron configuration should preferentially lead to 2n-transfer. The high intensity of the SPIRAL ^{6}He beams combined with the unique and high efficiency arrays like EXOGAM [9], the Neutron Wall [84] and EDEN [85] coupled to a Si telescope allowed the use of two independent techniques to explore the spatial configuration of the halo neutrons.

4.2.1. Transfer reactions in the ^{6}He+^{65}Cu system

Triple coincidence measurements, using intense (4×10^7 pps) ^{6}He beams, were used to study the neutron correlations by measuring the 1n and 2n cross sections in the ^{6}He+^{65}Cu system at 22.6 MeV [86]. The detection setup as shown in Fig 19a, consisted
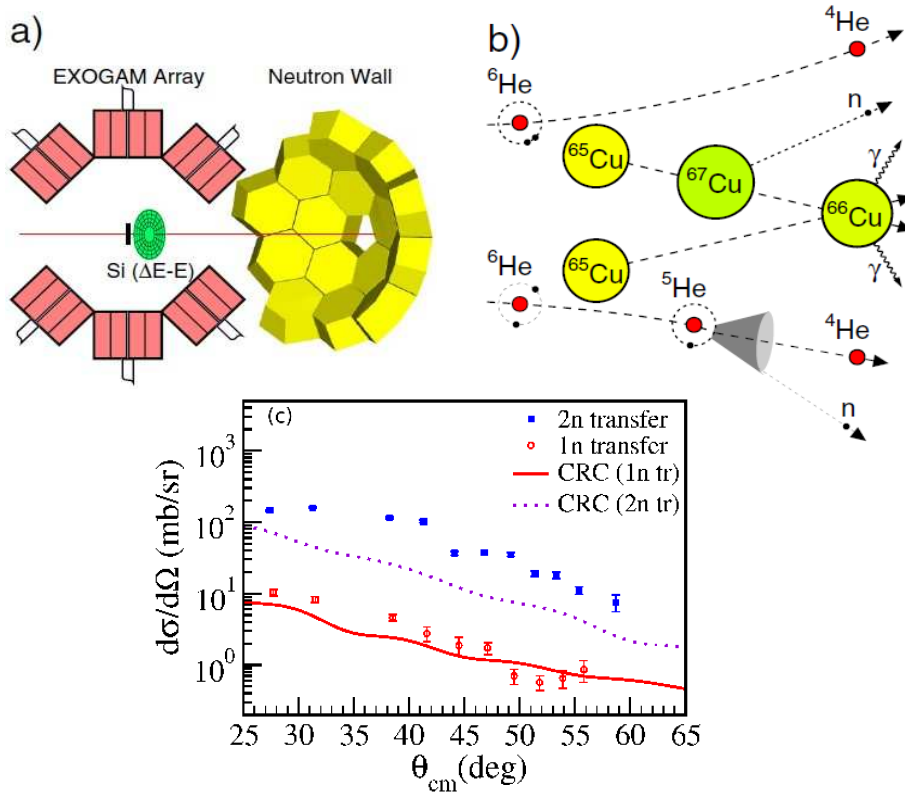
Figure 19. (colour online) Schematic view of (a) the experimental setup. (b) the reaction mechanism for the 2n- and 1n-transfer and (c) the angular distributions for 1n- and 2n-transfer. The corresponding CRC calculations for 1n and 2n-transfer are also shown.

of an annular Si telescope, the EXOGAM array [9] with 11 Compton-suppressed clovers, and a neutron array of 45 liquid scintillator elements [84]. The deconvolution of the $1n$- and $2n$- transfer contributions was obtained from the measured kinematic correlations between the energies and emission angles of the ^{4}He particles and neutrons (that exists for $1n$-transfer but not for $2n$-transfer) in coincidence with γ rays from the excited heavy residue. In the present case, 2n-transfer leads to the formation of ^{67}Cu with an excitation energy sufficient to evaporate a neutron (isotropically) forming ^{66}Cu. Owing to the Borromean nature of ^{6}He the final states are similar in both 1n- and 2n-transfer. In both cases the final state consists of a neutron, alpha particle and γ rays from the excited ^{66}Cu residue (Fig. 19b). As the emission of the neutron occurs via to different processes for 1n (the neutron arises from the breakup of ^{5}He) and 2n transfer (the neutron arises from the evaporation of an excited ^{67}Cu) a kinematic correlation (between the energies and emission angles) exists between the alpha particles and neutrons for 1n-transfer but not in the case of a 2n-transfer. Triple coincidences between neutrons and γ rays from the excited ^{66}Cu residues and alpha particles were used to deconvolute contributions
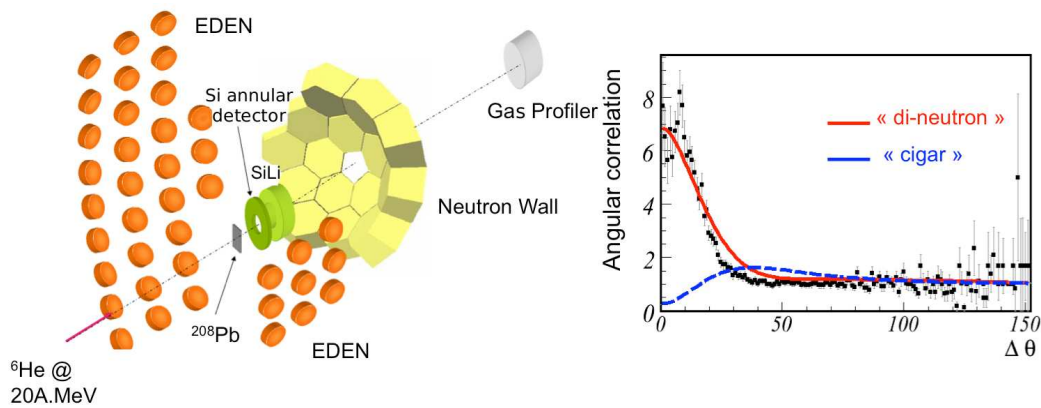
Figure 20. (colour online) Left Panel: Experimental setup for measuring the two neutrons produced in nuclear breakup in the ^{6}He+^{208}Pb system. Neutrons are detected in both the EDEN and Neutron Wall arrays. Right Panel: Measured angular correlation between the two neutrons emitted in coincidence (filled squares). The data are compared to microscopic calculations where the two nucleons are assumed to be either in a di-neutron like configuration (solid red line) using an attractive force between them or a cigar-like configuration (dashed blue line) using a repulsive force.

arising from 1n- and 2n-transfer and those arising from breakup of the projectile. This work showed the dominance of the 2n cross sections compared to 1n transfer cross sections, (Fig. 19c), thereby indicating the prevalence of the di-neutron structure in ^{6}He. Comparison with coupled reactions calculations for the angular distributions for transfer, elastic scattering and fusion illustrated the important role played by coupling to the two neutron channel in the reaction mechanism. Lower available beam intensities (two orders of magnitude) and the structure of ^{8}He preclude such direct measurements with ^{8}He beams today [87]. Therefore alternate methods will be required to study neutrons correlations in ^{8}He using re-accelerated beams.

4.2.2. Nuclear breakup in ^{6}He+^{208}Pb system

The nuclear breakup mechanism leading to the emission of the two neutrons in the continuum was also used to study the internal correlations of the two neutrons in the ^{6}He halo. The measurements were made using a 15 MeV/u ^{6}He beam on a ^{208}Pb target. By measuring the two neutrons in coincidence with the alpha particle ejectile (Fig. 20 left panel), the angular correlation between the two emitted neutrons initially in the "halo" was deduced [88]. Theoretical predictions based on the microscopic description of the evolution of two types of correlated systems (cigar or di-neutron correlation) suggest a large sensitivity to the initial correlation of the neutrons on the distribution of the relative angle between the neutrons following a nuclear breakup [89]. The right panel of Fig. 20 compares the experimental observations and theoretical predictions showing that the emission is compatible with two neutrons in the "halo" that are spatially close (di-neutron configuration). Both experiments discussed in this section, which employed independent approaches, indicate of a dominant di-neutron configuration in ^{6}He.

4.3. Tunnelling of exotic systems

Historically the alpha particle, the most stable bound helium isotope, played a pioneering role in the first application of the theory of quantum tunnelling. In this case a pure barrier penetration by a structureless object with a potential depending only on the distance between the centres of the interacting systems was considered. The helium isotopic chain provides a variety of properties to probe the effect of intrinsic structure and low binding energy on the tunnelling mechanism. Both ^{6}He and ^{8}He have low neutron separation thresholds and a Borromean structure. Contrary to the general trend, the measured charge radius of ^{8}He [8] has been found to be smaller than that of ^{6}He. This was attributed to a more isotropic distribution of the four valence neutrons around the alpha core. Furthermore, the increase of the neutron separation energy in ^{8}He compared to ^{6}He is opposite to the known behaviour for any other isotopic chain.

The helium isotopic chain is ideal for understanding the tunnelling of composite objects [90, 91, 92]. The ratio of masses, ρ, of interacting and non-interacting components (with respect to the Coulomb field) in a composite object, has been shown to play a significant role in low-energy reactions, such as increasing the tunnelling probability [92] (as seen, for example, in deuteron-deuteron reactions at keV energies [93]) and creating cusps and resonances [94]. The oscillations in the transmission coefficient have been shown to be damped with increasing ρ; such a result can also be inferred from Ref. [92]. In the neutron-rich helium isotopes the valence nucleons outside the alpha core can be treated as the "non-interacting" analog given the tight binding and point-like behaviour of the alpha particle. The helium chain offers a unique progression of ρ varying from 1 (^{8}He) and 2 (^{6}He) to the infinite limit for ^{4}He. In such a picture the helium isotopes are expected to behave differently with respect to their barrier penetration.

The availability of beams of such nuclei provides the opportunity to study the effect of exotic structures on the tunnelling mechanism. These relatively low beam intensities ($\sim 10^5$ pps) require employing techniques which are able to extract a weak signal in the presence of a relatively large background. The additional challenge in using in-beam measurements involving ^{8}He beams arise from the large gamma background associated with the beta decay of the beam. Activation techniques, when applicable, offer both a unique identification of the nucleus (obtained from the knowledge of the energy and half-life of the γ/α decay) and also a relatively lower background. To overcome the limitations of a low signal-to-noise ratio, a selective and sensitive method was designed to access the fusion cross sections. This involves the simultaneous measurement of X and γ rays emitted in electron capture decay of the evaporation residues [95]. A schematic view of the setup is provided in Fig. 21. The gain in sensitivity resulting from the present method, compared to an inclusive measurement, was found to be $\sim 3 \times 10^4$ in the region of interest. A typical γ-ray spectrum in coincidence with characteristic K_α X rays of Hg at $E_{\text{lab}} = 22.9$ MeV illustrating the selectivity of the method is also shown in the figure. This large gain in sensitivity can be put in perspective by noting out that
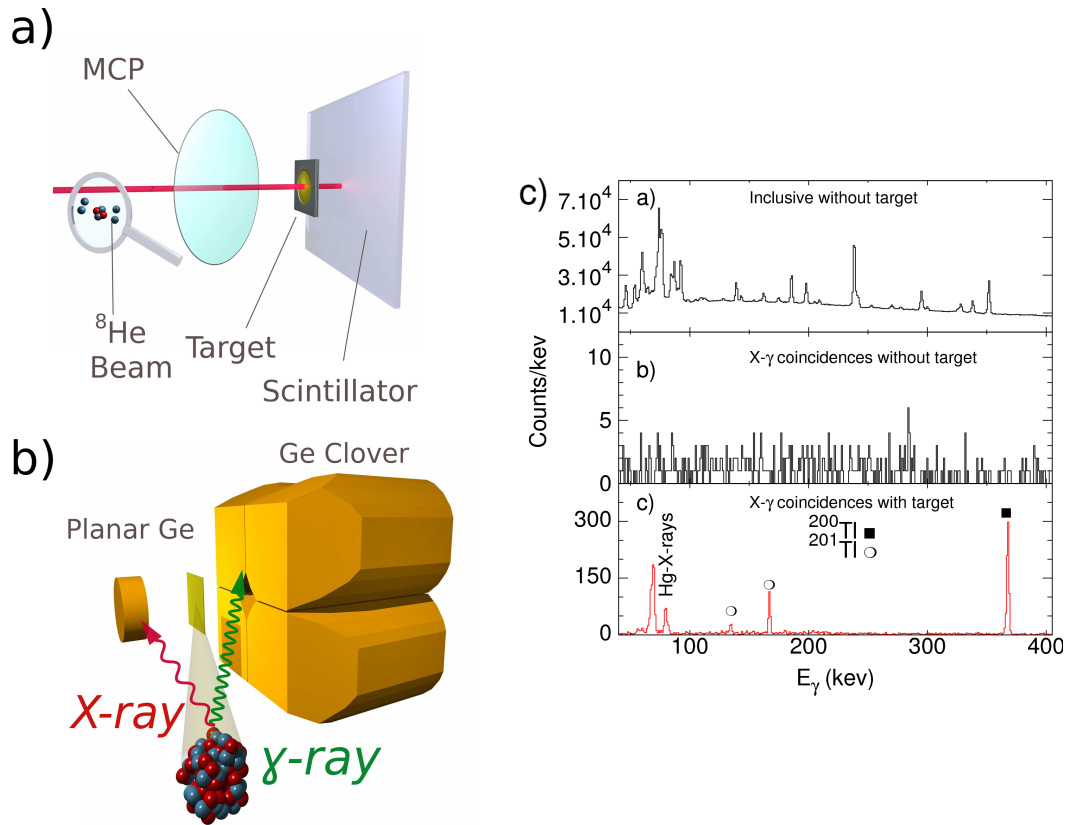
Figure 21. (colour online) Left: Schematic view of the experimental setup for a) in-beam and b) off-beam measurements. Right: a) γ-ray spectrum corresponding to a counting time of 210 h, without a target and any coincidence condition. (b) Same as (a) but requiring a coincidence condition on the region corresponding to the K_α X rays of Hg. (c) γ-ray spectrum in coincidence with characteristic K_α X rays of Hg with a target irradiated at $E_{lab} = 22.9$ MeV.

the smallest cross sections measured in this work using re-accelerated RIB, when scaled by the million times larger intensities available with stable beams, is comparable to the current measurement limits in nuclear physics.

The measured fusion cross sections for Helium isotopes with ^{197}Au [96, 97, 98] are shown in Fig. 22. The good agreement between the calculated and measured fusion cross section for ^{4}He [98] reinforces its point-like behaviour. At energies below the barrier the fusion cross sections, for ^{8}He and ^{6}He [97] are surprisingly similar and, as expected, are much larger than for ^{4}He [98]. A loosely bound system with a subsystem that does not feel the barrier can more easily restructure during the dynamical process of fusion, emphasizing the role of a flexible intrinsic wave function that can adiabatically readjust in a slow process and increase the barrier penetration. The observed similarity of the low-energy results for ^{8}He and ^{6}He may indicate the role of higher order processes with neutron-pair transfer preceding fusion. The most accurate and complete measurements
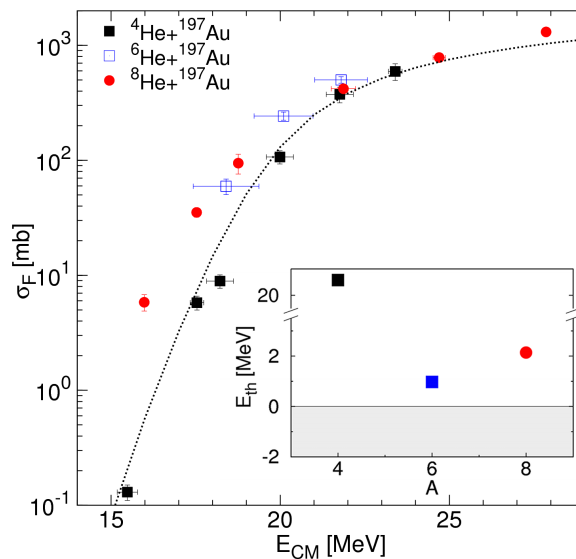
Figure 22. (colour online) Measured fusion cross section as a function of centre-of-mass energy E_{CM} for the ^{4,6,8}He + ^{197}Au systems [98, 97, 96]. The dotted line shows a one-dimensional barrier penetration calculation for ^{4}He + ^{197}Au. The inset shows the lowest threshold energy for He isotopes.

of ^{8}He+^{197}Au fusion and transfer [96] seem to indicate that for a loosely bound but essentially isotropic system like ^{8}He, it turns out to be easier to transfer part of the neutron excess in a peripheral reaction than to readjust the outer skin of the system and tunnel as a whole, a process which occurs only in a narrow region of small impact parameters. Understanding the intriguing behaviour of the helium isotopes may help possible future applications in the production of super heavy elements and the study of decoherence effects in open quantum systems [99]. The improved sensitivities demonstrated in this work using radioactive ion beams may also permit measurements which were earlier not possible.

4.4. Nuclear structure studies using γ-ray spectroscopy

Various techniques such as Coulomb excitation and fusion-evaporation are used to produce and characterize excited states in nuclei far from stability using reactions around the Coulomb barrier. These measurements were made using EXOGAM and when necessary in conjunction with auxiliary detectors including VAMOS, charged particle detectors and neutron detectors.

4.4.1. Coulomb excitation to probe nuclear shapes

Coulomb excitation at energies below the Coulomb barrier, is a purely electromagnetic process whereby multiple step processes can populate relatively high spin states. The excitation probabilities are to first order proportional to the square of the transitional matrix elements (B(E2) values). The second order reorientation effect introduces a
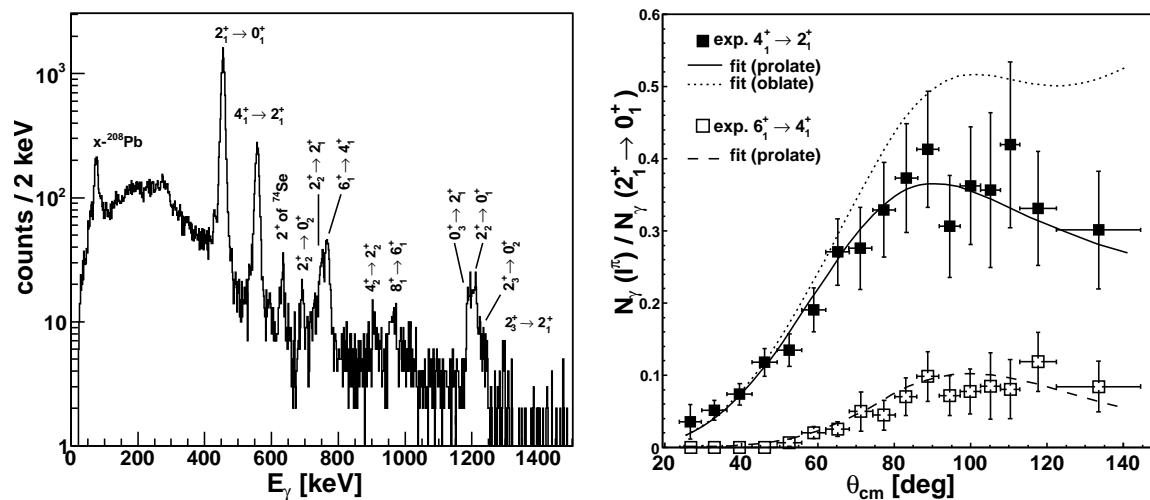
Figure 23. Left Panel: γ-ray spectrum obtained for the Coulomb excitation of ^{74}Kr.
Right Panel: The γ-ray yields for the $4^+ \to 2^+$ and $6^+ \to 4^+$ transitions, normalized
to the $2^+ \to 0^+$, are shown as a function of the centre of mass scattering angle. The
full line corresponds to a fit obtained with the GOSIA code [103], for a prolate ground
state of ^{74}Kr. To illustrate the sensitivity of the method for determining the sign of
the quadrupole moment, the is result of the calculation for an oblate shape (dotted
line) for the ground state.

dependence on the diagonal matrix element, allowing for the determination of the
static quadrupole moments and their signs [100]. Thus, Coulomb excitation studies
are sensitive to the distinction between prolate and oblate shapes. States of prolate
and oblate shape are likely to coexist within a narrow range of energy and are expected
to be strongly mixed. This feature of coexistence has been shown to arise from the
competition between large prolate or oblate proton and neutron shell gaps at $N = 34, 36$
and 38 in the ($Z = 36$, $N \simeq Z$) Kr isotopes [101]. The first experimental evidence of
such a shape coexistence in the light Kr isotopes was obtained from the observation of
low-lying excited states and their measured electric monopole decay strength $\rho(E0)$.
Additionally, the mixing between two 0^+ states induces a distortion in the regular
sequence of energies characterizing rotational bands of oblate or prolate rotors. This led
to the proposition [102] that, the ground states of ^{76,78}Kr are prolate, the prolate and
oblate shapes are strongly mixed in ^{74}Kr and the ground state configuration of ^{72}Kr is
mainly oblate. The experimental program carried out at SPIRAL aimed at determining
this evolution in shapes in the neutron deficient Kr isotopes. The EXOGAM array of
Ge clover detectors was coupled to a highly segmented annular Si detector to detect the
scattered particles in coincidence with the γ-ray transitions following the de-excitation
of states populated in Coulomb excitation.

High quality beams of $\sim 5 \times 10^5$ and 10^4 pps were used for the study of ^{76}Kr and
^{74}Kr nuclei, respectively. The gamma-ray spectrum obtained for ^{74}Kr exhibits many

transitions and is shown in Fig. 23 (higher statistics was obtained in the case ^{76}Kr). The excitation probabilities of several transitions were extracted from the γ-ray yields as a function of the scattering angle of the nuclei [104]. Both transitional and diagonal matrix elements were determined by fitting the observed yields. Negative values were found for the spectroscopic quadrupole moments of the first 2^+ states of ^{76}Kr and ^{74}Kr, indicating a prolate shape. The quadrupole moments of the $2^+_{2,3}$ states were found to be positive and the corresponding shape was interpreted to be oblate [104]. This result represents the first direct proof for a prolate-oblate shape coexistence in these nuclei. Comparison with calculations beyond the static mean-field approach emphasized the importance of including the triaxial degree of freedom to describe the shape coexistence in these nuclei [101, 105]. The present work was also the first exploitation of the reorientation effect with radioactive ion beams. Other transitional matrix elements between low-lying states were also extracted, providing information about the mixing of their wave functions. The nucleus ^{72}Kr is expected to be one of the few nuclei having an oblate ground state, however its study is presently not possible with the available intensity.

Similar studies undertaken were made in the case of ^{44}Ar [106] in order to gain an insight into the weakening of the N=28 shell closure and the development of deformation in this region. The first and the second 2^+ states in ^{44}Ar were populated in Coulomb excitation on ^{208}Pb and ^{109}Ag targets at beam energies of 2.68 and 3.68 MeV/u respectively. B(E2) values between all observed states and the spectroscopic quadrupole moment of the first 2^+ state were extracted from the differential Coulomb excitation cross sections. These results indicated a prolate shape for ^{44}Ar, demonstrating the onset of deformation for a nucleus already two protons and two neutrons away from doubly magic ^{48}Ca. Calculations were performed with the Gogny D1S interaction for ^{44}Ar and neighbouring nuclei using two different approaches: the angular momentum projected generator coordinate method considering axial quadrupole deformations and a five-dimensional approach including the triaxial degree of freedom. The experimental values were compared with new Hartree-Fock-Bogoliubov based configuration mixed shell-model calculations and also with shell-model and relativistic mean-field calculations. The calculations suggest a γ-vibrational character of the $2+_2$ state in ^{44}Ar [106].

4.4.2. Characterization of nuclei away from stability

Fusion and multi-nucleon transfer reactions using radioactive ion beams provide an alternate way to produce nuclei which are otherwise difficult to produce using stable beams. The low beam intensities and radioactive decay of the beam make inclusive measurements with RIB challenging. Here we discuss some of measurements that have been carried out.

The first experiment with the EXOGAM array, operated in a stand alone mode, used four detectors (in a "cube" geometry) to address the interplay between vibrational and multi-particle modes of excitation in neutron rich-nuclei around the doubly magic Pb. These nuclei are difficult to study at high spin due to the restricted possibilities with combinations of stable beams and targets. To overcome these constraints studies

were carried out using a ^{8}He beam on a thick ^{208}Pb target to investigate states in ^{212}Po and ^{213}At [107]. The measurements performed at a beam energy of 28 MeV with an intensity of 2×10^5 gave access to states up to a relatively high spin ($14\hbar$) in ^{212}Po. An increased relative population of states up to 12^+ was observed when compared with earlier work using a ^{208}Pb(^{9}Be,n)^{212}Po reaction at 48 MeV. Evidence for a previously unreported transition of 69 keV corresponding to $13 \to 12^+$ was found. States up to J^π = (39/2) were also observed in ^{213}At.

Gamma spectroscopy studies were also made near the proton drip line of the light rare earth elements. In particular, neutron deficient rare-earth nuclei around mass 130 are of great interest since highly deformed prolate ground states are predicted to exist in this region. These nuclei, with neutron numbers lying midway between the N= 50 and 82 shell closures and proton numbers away from the Z = 50 shell closure, are predicted to show very large ground-state deformations of $\beta_2 \sim 0.4$. Experimentally it was possible to populate and study with stable beams nuclei around A$\sim$130 only near, but not at the maximum of this predicted deformation. With this motivation, studies with fusion evaporation reactions using a ^{76}Kr beam, with intensities of 5×10^5 pps and an energy of 4.34 MeV/u on a ^{58}Ni target were made [109]. This experiment used the EXOGAM array in conjunction with VAMOS and the charged particle array DIAMANT [108] to enhance the selectivity of the relevant nuclei. The strong 4p exit channel populating ^{130}Nd, was studied up to relatively high spin and linear-polarisation measurements were also carried out. These early experiments demonstrate the potential of using fusion evaporation with low intensity RIB to populate and characterize states otherwise difficult to reach.

Multi-nucleon transfer reactions at energies around the Coulomb barrier allow to investigate among others the nucleon-nucleon correlation in nuclei, the transition from the quasi-elastic to the deep-inelastic regime and channel coupling effects in sub-barrier fusion reactions [112]. These reactions can also be used to produce and characterize nuclei far away from stability. Compared to reactions with stable beams where the main transfer channels are dominated by pick-up of neutrons and stripping of protons, those with radioactive ion beams open possibilities to populate nuclei by both the pick-up and stripping of protons and neutrons [111]. Thus not only neutron-neutron and proton-proton correlations but also the neutron-proton correlations can be studied simultaneously. The relevant information can be obtained from the observed population pattern of specific final states.

Studies of multi nucleon transfer were made using beams of ^{24}Ne on a Pb target at 7.9 MeV/u [113]. The light transfer products were detected and identified in VAMOS and the coincident gamma rays were detected using EXOGAM in a close packed geometry. Angular distributions for the elastic and inelastic channels were measured, together with distributions for the ^{23}Ne and ^{23}F channels. The relatively low beam intensity of 10^5 pps limited the population of more exotic channels. Angular distributions of a few channels were measured and found to be in rather good agreement with predictions from a semiclassical model. This work points to the potential of using

multi-nucleon transfer a probe of nuclear structure, with higher beam intensities.

The deexcitation of hot nuclei is generally understood using a statistical model. One of the important inputs is the knowledge of the level densities of the nuclei before and after particle emission, in particular the level density parameter a. To predict the decay of nuclei far from stability requires an understanding of the evolution of the level density. With this motivation measurements have also been made using SPIRAL beams to study the variation of the level density parameter as a function of isospin for nuclei around A=100. The level density parameter was investigated through the measurement of the evaporation residues using VAMOS in conjunction with characteristic K X-rays (for In nuclei) [114] and from the measurements of charged particles with the INDRA detector array [116] (Pd nuclei) [115]. The data are presently under analysis.

5. Nuclear Astrophysics

Radioactive ion beams play an important role in understanding how nuclear processes influence astrophysical phenomena. At SPIRAL taking advantage of the available high-quality post-accelerated beams two particular aspects have been addressed: (i) the role of unbound nuclei in explosive combustion of Hydrogen and (ii) the neutron capture cross section involving an unstable nucleus. Direct measurements of cross sections at low energies are also planned in the near future.

In explosive astrophysical environments such as X-ray bursters, dripline neutron-deficient nuclei can be strongly synthesized by fast and successive capture of protons. This leads to an equilibrium stage where the capture of another proton is followed by the instantaneous emission of a proton by the neighbouring proton-unbound nucleus. Such a waiting point can be bypassed by a two-proton radiative capture reaction if the final nucleus is bound. This is possible in several reactions, for example ^{15}O$(2p, \gamma)^{17}$Ne and ^{18}Ne$(2p, \gamma)^{20}$Mg. The exotic two-proton capture reaction was first proposed by Görres *et al.* [117]. These alternative paths can be calculated using the properties of the intermediate unbound nuclei (e.g. ^{16}F and ^{19}Na). Calculated reaction rates for two-proton capture were found to be significant only for astrophysical environments at very high densities. The properties of a large number of low lying states of the relevant unbound nuclei are presently unknown. Hence an experimental program was started with the objective to measure these properties with a high energy resolution and dedicated techniques to perform resonant elastic scattering were developed. These were first applied to measure the properties of the low lying states in ^{19}Na and ^{16}F. As mentioned earlier the beam energies provided by SPIRAL are ideal for transfer reactions (Sect.3). The (d,p) transfer reaction has been used to determine the important observables (Q values, excitation energy and spectroscopic factors) required to determine the (n,γ) radiative capture rate in the case of ^{46}Ar. This nucleus plays a pivotal role for understanding the reduction of ^{46}Ca with respect to ^{48}Ca in neutron capture - β-decay scenarios [118, 119]. The results of these measurements are presented in the following.

5.1. States in ^{19}Na

The focus of the first experiment made at the SPIRAL facility was the characterization of ^{19}Na through a measurement of the excitation function for the H(^{18}Ne, p)^{18}Ne reaction [120, 121]. A beam of ^{18}Ne^{4+} at 7.2 MeV/u and a purity of about 80% (20 % ^{18}O and < 1 % of ^{18}F) was purified using a stripper foil at the entrance of the LISE spectrometer. The resulting pure beam of ^{18}Ne^{10+}, with an intensity of 5x10^5 pps and target size of 3.8 x 1.7 mm (FW) was used for the measurement. A thick solid hydrogen cryogenic target [122] doubled as a beam stopper. The scattered protons from the thick target were detected at forward angles. A position sensitive Si telescope was used to identify and measure the energy of the light charged particles. The thick target made it possible to obtain a complete and continuous excitation function over a wide range of energies without changing the energy of the incoming beam. The H(^{18}O,p)^{18}O reaction was used to calibrate the detectors. The resulting ^{19}Na spectrum is shown in Fig. 24(a). Several broad peaks corresponding to new states in ^{19}Na can be seen.

The measured spectrum was analyzed using an R-matrix formalism to derive the energies, widths and spins of these states [121]. A large Thomas-Erhman shift of 725 keV was observed for the second excited state in ^{19}Na (the first peak in Fig. 24(a)). This was explained by Coulomb effects in the proximity of the proton emission threshold. The understanding of the decay process was crucial for interpreting the ^{19}Na excitation function. The measured two-proton events (Fig. 24(b)) explain the presence of two prominent peaks between 2 and 4 MeV. The efficiency for the detection of two-proton events at forward angles is enhanced by kinematic focusing inherent to the inverse kinematics. The two-proton events were interpreted to arise from sequential decays. Three new states with large widths were found in ^{19}Na (see figure 24(c)). A by-product of this work was the development of a new experimental method [123] based on proton-proton correlations to study inelastically excited states of the beam. Excited states and their decay modes in ^{18}Ne were also characterized from the analysis of the two proton events.

5.2. States in ^{16}F

The unbound system ^{16}F was studied using the method described above for ^{19}Na [124, 125]. A beam of ^{15}O at 1.2 MeV/u and an average intensity of 10^7 pps bombarded a 21μm thick polypropylene target. A beam contamination of less than 1 % of ^{15}N^{1+} was achieved using a stripper foil at the entrance of the LISE spectrometer. Two stable beams, ^{14,15}N obtained under similar experimental conditions were used for calibration purposes. Scattered protons were identified by their energy (5 keV resolution in the centre of mass frame) and time-of-flight. Figure 25(a) shows the measured excitation function, in the range from 0.450 MeV to 1.1 MeV, for the H(^{15}O,p)^{15}O reaction where three peaks can be seen. Since the energy resolution is proportional to $\tan(\theta_{lab})d\theta_{lab}$, protons were detected at zero degree with a restricted angular acceptance to achieve the best energy resolution. An energy resolution (FWHM) better than 5 keV in the centre
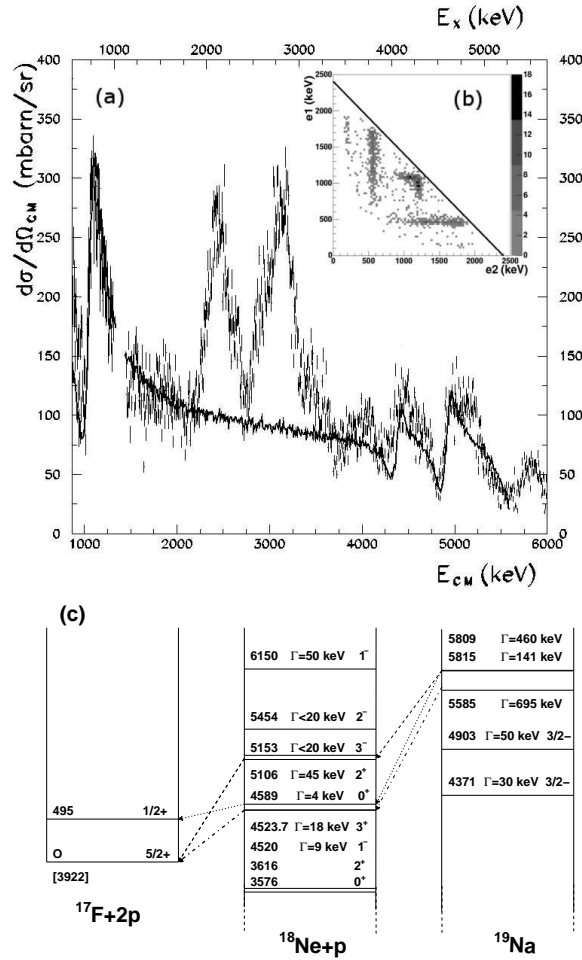
Figure 24. (a) Excitation function for the H(^{18}Ne,p)^{18}Ne reaction measured at 180°
in the centre of mass (C.M.). The line corresponds to an R-matrix calculation. (b)
Two proton emission H(^{18}Ne,2p)^{17}F was also observed. The energy of one proton is
plotted as a function of the energy of the second proton. (c) The level and decay
schemes of the relevant nuclei.

of mass was obtained (as far as we are aware this is the best energy resolution obtained
for charged particles involving RIB).

An R-matrix analysis was used to extract the properties of the first three states of
^{16}F necessary to calculate the two-proton capture reaction rates under astrophysical
conditions. Two new reaction channels ^{15}O(p,β^+)^{16}O and ^{15}O(p,γ)(β^+)^{16}O were
proposed to bypass the ^{15}O waiting point. Both reactions eventually proceed through
the β^+-decay of the intermediate unbound ground state of ^{16}F (Figure 25(b)), which
is fed directly by a proton capture or through a proton capture to the first excited
state followed by γ decay. Following the γ-emission to the low-energy tail of the ground
state resonance, the hindrance of the proton decay by the Coulomb barrier makes β
decay a competitive process. The cross section of these reactions were calculated by
considering the low energy tail of ^{16}F to be quasi-bound [124, 125]. The calculated
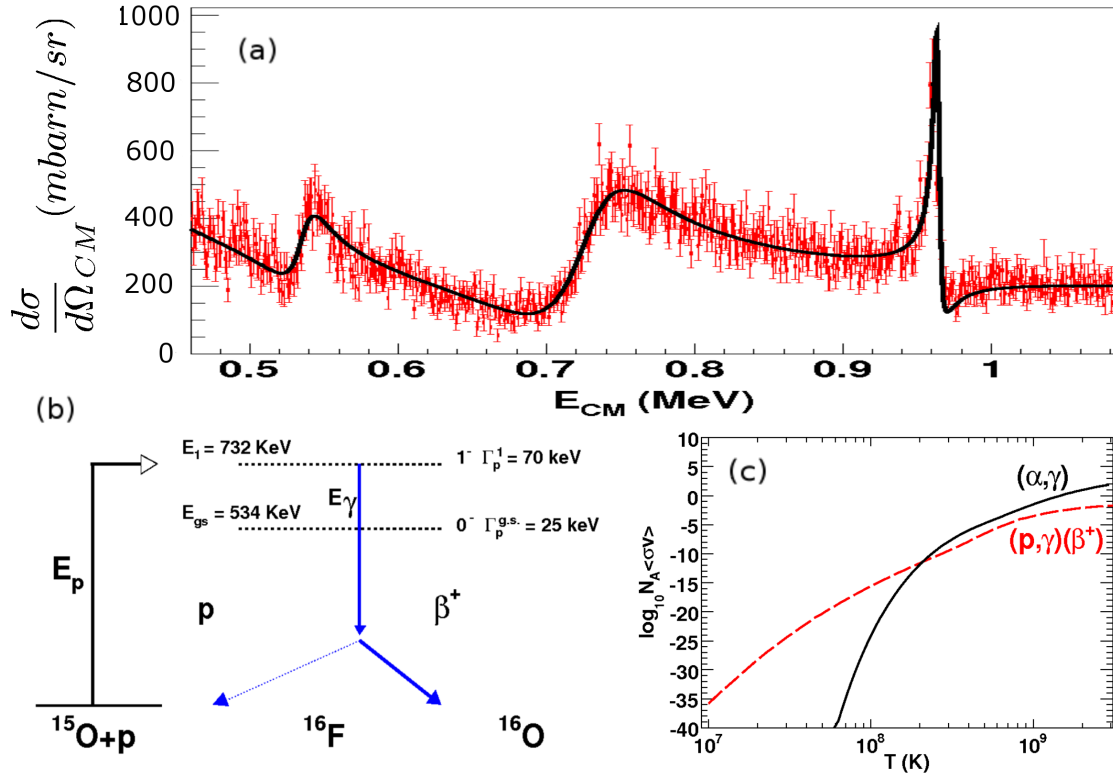
Figure 25. (colour online) (a) Excitation function for the H(^{15}O,p)^{15}O reaction measured at 180° in the centre of mass. The line corresponds to an R-matrix calculation. (b) Illustrating of possible new process proposed to bypass the ^{15}O waiting point. (c) Calculated reaction rates using the measured properties of ^{16}F.

reaction rates (Fig. 25(c)) indicate that the new proposed reactions can compete with the ^{15}O(α, γ)^{19}Ne breakout reaction.

5.3. Determination of the ^{46}Ar (n,γ) ^{47}Ar reaction rate

About two decades ago, Wasserburg and collaborators identified correlated isotopic anomalies for the neutron-rich ^{48}Ca, ^{50}Ti and ^{54}Cr isotopes in certain refractory inclusions of the Allende meteorite [126, 127]. For example, the ^{48}Ca/^{46}Ca ratio was found to be 250, a factor of 5 larger than observed in the solar system. It was concluded that these highly unusual isotopic compositions were witness to late-stage nucleosynthesis processes which preceded the formation of the solar nebula. However, astrophysical models existing at that time encountered severe difficulties when trying to reproduce these observed anomalies, in particular those in the EK-1-4-1 inclusion. A plausible astrophysical scenario to account for the overabundance of ^{48}Ca is a weak rapid neutron-capture process [118, 128]. In such a scenario the neutron-rich stable ^{46,48}Ca isotopes are produced during a neutron-capture and β-decay process from lighter-Z
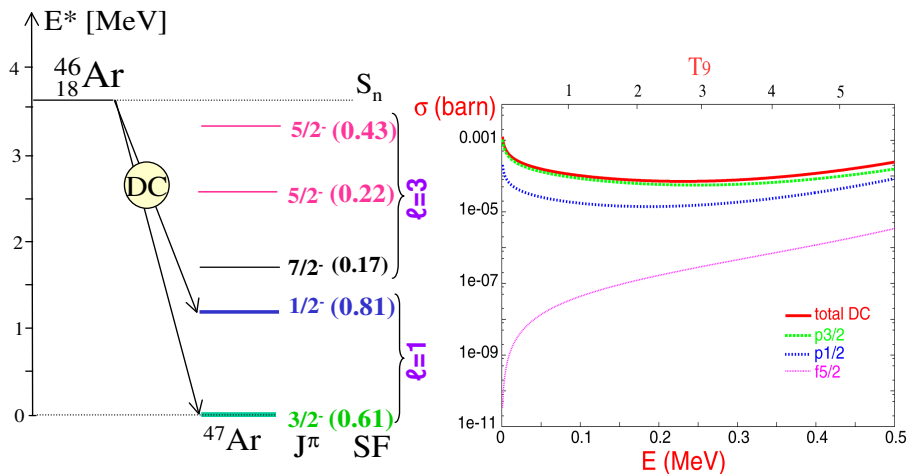
Figure 26. (colour online) Left: Experimental level scheme of ^{47}Ar as a function of the excitation energy E*. The main levels which contribute to the neutron-capture are represented with their angular momenta ℓ and J and spectroscopic factors (in parenthesis). Right: Calculated σ_n as a function of the stellar temperature in units of 10^9K (top axis) or as a function of the neutron energy (bottom axis) for the three levels indicated. The total cross section is shown in red.

stable seed nuclei. The main contribution to the production of these Ca isotopes is provided by the β-decay of their progenitor isobars in the Ar isotopic chain [118, 119]. This hypothesis was derived from the fact that, in the $Z < 18$ chains, the measured β-decay lifetimes of ^{44}S and ^{45}Cl are shorter than the neutron-capture rates at the $N = 28$ shell closure. Consequently, the matter flow in the S and Cl chains is depleted by β-decay to the higher Z isotopes before reaching masses A=46 or 48. Thus the main progenitors of ^{46,48}Ca are produced either directly in the Ar chain or from the β-decay of $Z < 18$ nuclei which could subsequently capture neutrons in the Ar chain. Therefore, the determination of neutron-capture rates in the Ar isotopes is important. Indeed, a high neutron-capture rate at A=46 would reduce drastically the amount of progenitors of ^{46}Ca as the neutron-capture quickly shifts the matter flow to A=48, enriching ^{48}Ca accordingly. In the following, the ^{46}Ar(d,p)^{47}Ar reaction is used as a "surrogate" to determine the ^{46}Ar(n,γ)^{47}Ar reaction rate.

The ^{46}Ar nucleus lies at the N=28 shell closure, where a sudden drop of the neutron-separation energy is expected to lead to a change in the Q value for the neutron-capture cross section, despite the reduction of the shell gap. Consequently, the ^{46}Ar(n,γ)^{47}Ar capture cross section (σ_n) is, a priori, expected to be small as compared to neighbouring nuclei. In the present case of low nuclear density and where bound p states are present, the neutron capture occurs principally through direct capture to bound states (DC). Taking into account the conservation of spin in the reaction, the neutron is captured in ℓ=1 bound states through the E1 operator without a centrifugal barrier, as the transferred angular momentum is ℓ_n=0 (s-wave capture). As shown in Fig. 26, the ratio between an s-wave (final state with ℓ=1) and d-wave (final state with ℓ=3) direct neutron capture rate is approximately 10^4 at a stellar temperature of 10^9K. This arises

from the influence of the centrifugal barrier which strongly hampers neutron-capture on orbits with higher angular momenta. Therefore, the contribution of direct capture to the g.s. and first excited states, both having a large spectroscopic factors $\ell=1$, dominate. This gives rise to large neutron capture cross sections for A=46, ^{46}Ar, leading to a small depletion through β-decay at A=46 as the lifetime of ^{46}Ar (7.85 s) is longer than the neutron capture (t_n). At A=48, t_n becomes much longer than t_β. It follows that neutron captures are halted in the Ar chain at A=48, accumulating a substantial amount of ^{48}Ca. These two features can explain the high ^{48}Ca/^{46}Ca ratio for a stellar temperature of 10^9K and a neutron density d_n of 6 $\times 10^{19}$/cm^3.

6. Summary and Perspectives

A large and varied program, using a range of direct and compound processes with re-accelerated beams from SPIRAL in range of 1.2 to 20 MeV/u, to address several important questions in nuclear physics, has been presented. Such a program also necessitated the development of a variety of state-of-the art detectors, such as the active target MAYA, the charged particle detectors like MUST/MUST2 and TIARA, the EXOGAM Ge array and the versatile high acceptance spectrometer VAMOS. In the coming years GANIL concentrate its development and research activities on ISOL with the commissioning of the SPIRAL2 facility [130]. The wide ranging capabilities at GANIL will also continue to be maintained, also keeping in mind that the post acceleration of fission fragment beams at higher energies could be one possible future avenue for the facility. In the near future, beams available at SPIRAL are planned to be extended [129]. In particular, the use of hot 1^+ ion-sources, such as surface ionization cavities (already tested) and FEBIAD sources developed at CERN, are envisaged to enable the production of alkali and metallic beams having melting points up to 2000°K. These, in conjunction with an ECR charge breeder (tested on-line at CERN ISOLDE), are expected to provide post accelerated beams with A $\leq$ 100 up to energies of 10 MeV/u. In this scenario with the present graphite targets, neutron deficient beams such as ^{38}Ca should also be possible with intensities $\leq 10^4$ pps. In a longer term perspective, the use of target materials having a higher Z should permit the production of isotopes of heavier elements ranging from Sn up to Ta.

SPIRAL2 [130] is a major expansion of the SPIRAL facility, and represents a significant element in European ISOL development program. The main goal of SPIRAL2 is to extend the knowledge of the limit of existence and the structure of nuclei far from stability to presently unexplored regions of the nuclear chart, in particular in the medium and heavy mass region (60$\leq$A$\leq$140). SPIRAL2 is based on a high power, CW, superconducting driver LINAC, delivering up to 5 mA of deuteron beams at 40 MeV (200 kW) which will impinge on a C converter + Uranium target to produce more than 10^{13} fissions/s. The expected radioactive ion beam intensities for exotic species in the mass range from A=60 to A=140, are of the order of $10^6 - 10^{10}$ pps. These beams will be available at energies between a few keV/u (at the dedicated
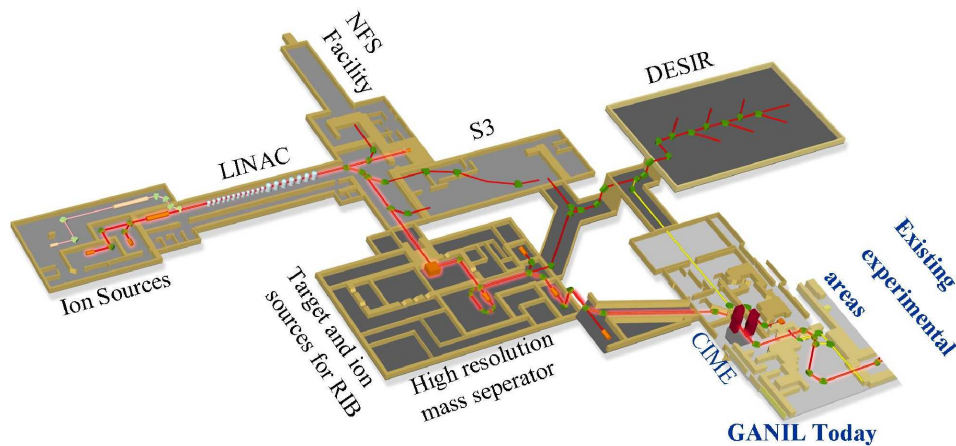
Figure 27. (colour online) The evolution of the GANIL facility compared to that shown in Fig. 1, showing the various components of the SPIRAL2 facility.

DESIR facility) and 10 MeV/u (after post acceleration by the CIME cyclotron) in the current experimental halls. The same driver will also be used to accelerate high intensity (100μA to 1 mA), light and heavy ions up to 14.5 MeV/u to produce neutron deficient and very heavy exotic nuclei. In the first phase the intense stable beams from the LINAC will be used in conjunction with the high rejection S3 spectrometer [131] to study heavy and super heavy nuclei and to produce a high flux of neutrons in the energy range of 1-40 MeV at the NFS (Neutrons for Science) facility. A broad range of next generation instrumentation, including the PARIS gamma-array, the upgrade of EXOGAM electronics (EXOGAM2) and the FAZIA and GASPARD charged particle arrays are being planned to exploit the high intensity radioactive ion beams. Suitable changes to the existing facility to account for safety regulations related to the use of these high intensity beams are in progress. The first intense beams from the LINAC and the re-accelerated beams of fission fragments are expected in 2012 and in 2014 respectively. The SPIRAL2 project will substantially increase technical know-how of technical solutions that will contribute to EURISOL [132] and other projects around the world. With the completion of the SPIRAL2 project a wide diversity of beams with energies ranging from a few keV to 95 MeV/u coupled to broad array of detection systems will be available at GANIL. The entire accelerator complex will be able to provide up to five stable and/or radioactive ion beams simultaneously. Such developments hold promise in advancing our understanding of the origin of simple patterns in complex nuclei.

Acknowledgments

References

[1] R. Anne and A.C. Mueller 1992 *Nucl. Instrum. Methods Phys. Res.* B **70** 276

[2] A. Joubert *et al.* 1991, Proc. of the Second Conf. of the IEEE Particle Accelerator, San Francisco U.S.A, 594; *ibid Nucl. Phys. News* 1990 **1** 3

[3] O. Kofoed-Hansen and K.O. Nielsen 1951 Phys. Rev. 82 96

[4] M. Huyse and R. Raabe, contribution to this Focus Section

[5] A.C.C. Villari 2001 *Nucl. Phys. A* **693** 465; A.C.C. Villari *et al.* 2003 *Nucl. Instrum. Meth. Phys. Res.* B **204** 173; A.C.C. Villari *et al.* 2007 *Nucl. Phys. A* **787** 126c

[6] L. Maunoury *et al.* 1997 13th Int. Workshop on ECR Ion Sources, College Station, Texas, USA.

[7] X. Flechard *et al.* 2008 *Phys. Rev. Lett.* **101** 212504

[8] P. Mueller *et al.* 2007 *Phys. Rev. Lett.* **99** 252501

[9] J. Simpson *et al.* 2000 *Heavy Ion Phys.* **11** 159

[10] H.Savajols for the VAMOS collaboration 1999 *Nucl. Phys. A* **693** 1027c

[11] S. Pullanhiotan *et al.* 2008 *Nucl. Instrum. Meth. Phys. Res. A* **593** 343

[12] Y. Blumenfeld *et al.* 1999 *Nucl. Inst. Meth. Phys. Res. A* **421** 471

[13] E.C. Pollacco *et al.* 2005 *Eur. Phys. J.* A **25** 287

[14] M. Labiche *et al.* 2010 *Nucl. Instrum. Meth. Phys. Res. A* **614** 439

[15] C.E. Demonchy *et al.* 2007 *Nucl.Inst. Meth. Phys. Res. A* **583** 341

[16] G. Wittekar *et al.* 2005 Real Time Conference 14th IEEE-NPSS

[17] S. Bhattacharyya *et al.* 2008 *Phys. Rev. Lett.* **101** 032501; A. Shrivastava *et al.* 2009 *Phys. Rev..* C **80** 0515305(R)

[18] C. Schmitt *et al.* 2010 *Nucl. Instrum. Meth. Phys. Res. A* **621** 558

[19] C. Unsworth *et al.* 2009 *Nucl. Instrum. Meth. Phys. Res. A* **604** 67

[20] http://pro.ganil-spiral2.eu/laboratory/detectors/exogam

[21] L. Bianchi *et al.* 1989 *Nucl. Instrum. Meth. Phys. Res. A* **276** 509

[22] S. Ottini-Hustache *et al.* 1999 *Nucl. Instr. Meth. Phys. Res. A* **431**, 476

[23] P. Baron *et al.* 2003 *Nucl. Science Symposium Record.* IEEE Vol **1** 386

[24] J.C Santiard *et al.* 1994 *CERN-ECP/* **94-17**

[25] O. Sorlin and M.-G. Porquet 2008 *Prog. Part. Nucl. Phys.* **61** 602

[26] Y. Utsuno *et al.* 1999 *Phys. Rev. C* **60** 054315

[27] T. Otsuka *et al.* 2002 *Eur. Phys. J* A **15** 151

[28] M. Stanoiu *et al. 2004 Phys. Rev.* C **69** 034312

[29] W. Catford *et al.* 2010 *Phys. Rev. Lett.* **104** 192501

[30] J.R. Terry *et al.* 2004 *Nucl. Phys. A* **734** 469

[31] http://www.nscl.msu.edu/ brown/resources/SDE.HTM

[32] B. A. Brown and W. A. Richter 2006 *Phys. Rev. C* **74** 034315

[33] A. Obertelli *et al.* 2006 *Phys. Lett.* B **633** 33

[34] J.R. Terry *et al.* 2006 *Phys. Lett.* B **640** 86

[35] S. Brown 2010 PhD Thesis, University of Surrey U.K

[36] B. Fernandez-Dominguez, Private communication

[37] A. Ramus *et al.* 2009 *Int. Jour. of Mod. Phy.* E **18** 2056; A. Ramus PhD Thesis 2009 Université Paris XI

[38] T. Otsuka *et al.* 2010 *arXiv :0908.2607v2 [nucl-th]*

[39] L. Gaudefroy *et al.* 2008 *Phys. Rev. C* **78** 034307

[40] L. Gaudefroy *et al.* 2006 *Phys. Rev. Lett.* **97** 092501; L. Gaudefroy *et al.* 2007 *Phys. Rev. Lett.* **99** 099202

[41] S. Nummela *et al.* 2001 *Phys. Rev. C* **63** 044316

[42] R. Abegg *et al.* 1978 *Nucl. Phys. A* **303** 121

[43] Y. Uozumi *et al.* 1994 *Nucl. Phys. A* **576** 123

[44] P. D. Cottle *et al* 1998 *Phys. Rev. C* **58** 3761

[45] T. Otsuka *et al.* 2005 *Phys. Rev. Lett.* **95** 232502

[46] B. G. Todd-Rutel *et al.* 2004 *Phys. Rev. C* **69** 021301(R)

[47] L. Gaudefroy *et al.* 2009 *Phys. Rev. Lett.* **102** 092501

[48] S. Grévy *et al.* 2005 *Eur. Phys. J. A* **25** s01 111

[49] B. Bastin *et al.* 2007 *Phys. Rev. Lett.* **99** 022503

[50] Z. Dombràdi *et al.* 2003 *Nucl. Phys. A* **727** 185

[51] F. Skaza *et al.* 2005 *Phys. Lett.* B **619** 82

[52] F. Skaza *et al.* 2006 *Phys. Rev.* C **73** 044301

[53] N. Keeley *et al.* 2007 *Phys. Lett.* B **646** 222

[54] A. Korsheninnikov *et al.* 2003 *Phys. Rev. Lett.* **90** 082501

[55] L.V. Chulkov *et al.* 2005 *Nucl. Phys. A* **759** 43

[56] X. Mougeot, PhD Thesis 2009, Universite Paris XI IRFU-08-06-T; X. Mougeot *et al.*, in preparation

[57] T. Otsuka *et al.* 2001 *Phys. Rev. Lett.* **87** 082502

[58] S. Fortier *et al.* 2007 Proc. Int. Symposium on Exotic Nuclei, Khanty-Mansiysk, Russia, July, 2006, Yu.E.Penionzhkevich, E.A.Cherepanov, Eds. AIP Conf. Proc. **912** 3

[59] K.K. Seth *et al.* 1987 *Phys. Rev. Lett.* **58** 19

[60] H.G. Bohlen *et al.* 1988 *Z. Phys. A* **330** 22; H. G. Bohlen *et al.* 1999 *Prog. Part. Nucl. Phys.* **42** 17

[61] L. Chen *et al.* 2001 *Phys. Lett.* B **505** 21

[62] H. Al Falon, 2007, PhD. Thesis, University of Caen, LPCC T07-02

[63] H.T. Johansson *et al.* 2010 *Nucl. Phys. A* **842** 15

[64] M. Golovkov *et al.* 2007 *Phys. Rev. C* **76** 021605 (R)

[65] M. Caamano *et al.* 2007 *Phys. Rev. Lett.* **99** 062502

[66] M. Caamano *et al.* 2008 *Phys. Rev. C* **78** 044001

[67] C. Détraz *et al.* June 1990 experiment proposal E169 GANIL

[68] F. M. Marques *et al.* 2002 *Phys. Rev. C* **65** 044006

[69] F.M. Marques *et al.* 2005 arXiv:nucl-ex/0504009v1

[70] N.A. Orr and M. Marques 2009 private communication

[71] E. Rich *et al.* 2005 Proc. Int. Symposium Exotic Nuclei, Peterhof, Russia, Yu.E.Penionzhkevich, E.A.Cherepanov, Eds., World Scientific, Singapore, 36

[72] S. Pieper 2003 *Phys. Rev. Lett.* **90** 252501

[73] R. Lazauskas and J. Carbonel 2005 *Phys. Rev. C* **72** 034003

[74] L.F. Canto, P.R.S. Gomes, R. Donangelo, M.S. Hussein 2006 *Phys.Rep.* **424** 1

[75] N. Keeley, N. Alamanos, K. W. Kemper, and K. Rusek 2009 *Prog. Part. Nucl. Phys.* **63** 396

[76] K. Hagino, A. Vitturi, C.H. Dasso, S.M. Lenzi 2000 *Phys. Rev.* C **61** 037602

[77] A. Navin *et al.* 2004 *Phys. Rev. C* **70** 044601

[78] R. Raabe *et al.* 2004 *Nature(London)* **431**, 823

[79] A. Lemasson *et al.* 2010 *Phys. Rev. C* **82** 044617

[80] D. Hinde and M. Dasgupta 2004 *Nature* **431** 748

[81] A Di Pietro *et al.* 2004 *Phys. Rev. C* **69** 044613

[82] K. Hagino *et al.* 2009 *Phys. Rev. C* **80** 031301

[83] W. von Oertzen and A. Vitturi 2001 *Rep. Prog. Phys.* **64** 1247

[84] O. Skeppsted *et al.* 1999 *Nucl. Inst. Meth. A* **421** 531

[85] H. Laurent *et al.* 1993 *Nucl. Inst. Meth. A* **326**

[86] A. Chatterjee *et al.* 2008 *Phys. Rev. Lett.* **101** 032701

[87] A. Lemasson *et al.* 2010 *Phys. Lett.* B (submitted)

[88] M. Assié *et al.* 2009 *Eur. Phys. J A* **42** 441

[89] M. Assié and D. Lacroix 2009 *Phys. Rev. Lett.* **102** 202501

[90] C. A. Bertulani,V. V. Flambaum, and V. G. Zelevinsky 2007 *J. Phys. G: Nucl. Part. Phys.* **34** 2289

[91] S. Bacca and H. Feldmeier 2006 *Phys Rev. C* **73** 054608

[92] M. R. A. Shegelski, J. Hnybida, and R. Vogt 2008 *Phys. Rev.* A **78** 062703

[93] H. Yuki *et al.* 1998 JETP Lett. **68** 823

[94] N. Ahsan and A. Volya, 2008 *Nuclear Many-Body Physics Where Structure and Reactions Meet* (World Scientific, 2008) 539; N. Ahsan and A. Volya 2010 arXiv:1010.3973

[95] A. Lemasson *et al.* 2009 *Nucl. Inst. Meth.* A **598** 445

[96] A. Lemasson *et al.* 2009 *Phys. Rev. Lett.* **103** 232701

[97] Yu. E. Penionzhkevich *et al.* 2007 *Eur. Phys. J.* A **31** 185

[98] M. S. Basunia, H. A. Shugart, A. R. Smith, E. B. Norman 2007 *Phys. Rev.* C **75** 015802

[99] D. Hinde *et al.* 2010 *Nucl. Phys.* A **844** 117c

[100] A. Görgen 2010 *J. Phys. G: Nucl. Part. Phys.* **37** 103101

[101] M. Bender, P. Bonche and P. -H. Heenen 2006 *Phys. Rev. C* **74** 024312

[102] E. Bouchez *et al.* 2003 *Phys. Rev. Lett.* **90**, 082502

[103] T. Czosnyka, D. Cline and C. Y. Wu 1983 *Bull. Am. Phys. Soc.* **28** 745

[104] E. Clément *et al.* 2007 *Phys. Rev. C* **75** 054313

[105] M. Girod, J.-P. Delaroche, A. Görgen, A. Obertelli 2009 *Phys. Lett.* B **676** 39

[106] M. Zielinska *et al.* 2009 *Phys.Rev.* C **80** 014317

[107] A. B. Garnsworthy *et al.* 2005 *J. Phys. G: Nucl. Part. Phys.* **31** S1851

[108] J.N. Scheurer *et al.* 1997 *Nucl. Instr. and Meth.* A **385** 501

[109] M. Petri *et al.* 2006 *Phys. Scr.* **T125** 214

[110] M. Petri *et al.* 2009, *Nucl. Inst. Meth.* A **607** 412

[111] C.H. Dasso, G. Pollarolo and A. Winther 1994 Phys. Rev. Lett. **73** 1907

[112] L. Corradi, G. Pollarolo and S. Szilner 2009 *J. Phys. G: Nucl. Part. Phys.* **36** 113101

[113] G. Benzoni *et al.* 2010 *Eur. Phys. J.* A **45** 287

[114] M. Morjean *et al.* 2009 Private communication

[115] N. Le Neindre for the INDRA collaboration 2009 Private communication

[116] J. Pouthas *et al.* 1995 *Nucl. Instrum. Meth. Phys. Res.* A, **357** 418

[117] J. Görres *et al.* 1995 Phys. Rev. C **51** 392

[118] O. Sorlin *et al.* 2003 *C. R. Physique* **4** 541

[119] L. Gaudefroy *et al.* 2006 *Eur. Phys. J.* A **27** s01 302

[120] A. C. C. Villari and F. de Oliveira Santos 2002 *Nuclear Physics News* **12** 29

[121] F. de Oliveira *et al.* 2005 *Eur. Phys. J.* A **24** 237

[122] P. Dolegieviez *et al.* 2006 *Nucl. Instrum. Methods Phys. Res.* A **564** 32

[123] J.C. Dalouzy *et al.* 2009 *Phys. Rev. Lett.* **102** 162503

[124] I. Stefan *et al.* 2006 Tours Symposium on Nuclear Physics, AIP Conference Proceedings Volume 891 155

[125] F. de Oliveira Santos and the E400S collaboration 2007, International Conference-PROCON 2007, AIP Conf. Proc. **961** 205

[126] T. R. Lee *et al.* 1978 *Ap. J.* **220** L21

[127] F. R. Niederer *et al.* 1980 *Ap. J.* **240** L73

[128] K. -L. Kratz *et al.* 2001 *Mem. Soc. Astronom. Ital.* **72** N2 453

[129] M. G. St-Laurent *et al.* 2010 International Symposium on Exotic Nuclei (EXON2009), Sochi Russia, AIP Conference Proceedings 1224 482; F. Chautard 2010 in the Proc. of the 19th Int. Conference on Cyclotron and their Application, Sept 6-10 2010 Lanzhou ,China

[130] http://pro.ganil-spiral2.eu/spiral2

[131] http://pro.ganil-spiral2.eu/spiral2/instrumentation

[132] Y. Blumenfeld *et al.* 2009 *International Journal of Modern Physics* E **18** 1960.